博士論文

Study of magnetic-field-induced phase transitions in correlated spin systems using megagauss magnetic fields

（メガガウス磁場を用いた相関スピン系における磁場誘起相転移の研究）

周　旭光

Study of magnetic-field-induced phase transitions in correlated spin systems using megagauss magnetic fields
(メガガウス磁場を用いた相関スピン系における磁場誘起相転移の研究)

Xu-Guang Zhou
(周 旭光)

Superviser: Yasuhiro H. Matsuda
(松田　康弘)

Ph. D Degree Thesis

Department of Advanced Material

University of Tokyo

Abstract

The theory of spin of electrons was developed by Heisenberg after the experimental discovery that the particles have an intrinsic angular momentum. Correlation between spins is determined by the exchange interactions, and the quantum mechanics governs behavior of the spins especially in systems with a small spin quantum number such as 1/2 and 1. Such a system is sometimes termed quantum spin system. In addition, many-body effects described with the Hubbard model can be reduced to the Heisenberg Hamiltonian and the magnetic properties of the strongly correlated electron system such as the Mott insulator is understood through the Heisenberg spin model. I define the quantum spin systems and the strongly correlated electron systems as the correlated spin system (CSS) in this thesis.

In some low dimensional CSSs(1,2-dimensional system), models based on the theory of spin are particularly fruitful because their simplicity has enabled exact solutions to be found which contain many highly non-trivial features. Furthermore, there are many cases, for example 3-dimensional spin systems, in which we can find no exact solution; these cases can be used as a testing ground for approximate methods of modern quantum mechanics using the spin models. By increasing ability of solid-state experimentalists to fashion magnetic systems of various dimensionalities, the experimental major boosts have come from the various measurements of the CSSs, including but not limited to magnetization, neutron, electron spin resonance (ESR) and nuclear magnetic resonance (NMR). It is fair to say that almost all interesting features of quantum many-body physics are found in quantum spin models; various kinds of phase transitions, role of symmetries and spontaneous symmetry breaking, quantum phases of matter such as Bose-Einstein condensation (BEC) and superfluidity, valence bond solids, magnetic plateau, superconductivity, the integer and fractional quantum Hall effects, topological order, exotic quasi-particles called anyons etc..

The importance of magnetic field in studying CSS is obvious. Research on quantum spin systems is usually limited to a magnetic field of less than 60 T in that the relatively easy implementation of external magnetic field is possible. However, in many CSSs, a higher magnetic field is required to observe significant field-induced effects because of the large energy scale of the interaction. CSSs with large energy scale interactions are often a better choice or even only the choice for studying a given theoretical quantum spin model such as the case of an orthogonal-dimer antiferromagnet $SrCu_2(BO_3)_2$. In this study, we have focused on three materials, $TlCuCl_3$, α-$RuCl_3$ and YbB_{12}, and studied the property of magnons' Bose-Einstein condensation, spin liquid and Kondo insulator, respectively. Actually, I perform experiments of magnetization or magnetoresistance measurements in a megagauss external magnetic field (> 100 T).

In the first study, the magnetization process of $TlCuCl_3$ is studied. $TlCuCl_3$ is a 3-dimensional gapped spin-1/2 dimer system. An image of a simple Zeeman splitting of the spin-triplet state is helpful to understand the magnetic process of the spin dimer system. In a pure dimer system, the transition between singlet state and the $S_z = 1$-triplet state under an external magnetic field drives a phase transition at the critical magnetic field $H_g = \Delta/\mathrm{g}\mu_B$, where Δ is the spin gap energy. The H_g separates into two distinct critical points H_{c1} and H_{c2} in real spin gap materials due to inter-dimer interactions; these two critical magnetic fields correspond to the beginning and saturation of the magnetization, respectively. In previous studies, it has been proposed that the field-induced ordering phase in $TlCuCl_3$ can be interpreted as a BEC phase of magnons. On the other hand, detailed experimental measurements of $TlCuCl_3$ at the high-field side near H_{c2} have been lacking because of its large H_{c2} (up to ∼100 T) due to the strong inter-dimer interaction in $TlCuCl_3$. In some other gapped spin dimer systems, which possess weak inter-dimer interaction, like $BaCuSi_2O_6$, the properties of H_{c2} have been investigated by means of a projection from the spin model, the so-called hard-core boson model. Based on the results of hard-core boson model, the magnetic-field dependence of the order parameters in phase diagrams has a symmetry with respect to the particle-hole invariant point $H = (H_{c1} + H_{c2})/2$. Such a symmetry is reflected by the mirror symmetry observed in the shape of the phase boundary of the BEC phase in $BaCuSi_2O_6$. However, this particle-hole symmetry of the phase boundary in $TlCuCl_3$ is expected to be broken because the conditions of the hard-core boson picture are not satisfied. We discuss the particle-hole symmetry breaking of the BEC phase using the experimental result of entire magnetization process of $TlCuCl_3$ up to 100 T. Theoretical calculations with Quantum Monte Carlo (QMC) method and bond operator theory are also performed for detailed discussion on the particle-hole symmetry breaking.

The second work studied is the field-angle dependence of the phase diagram of α-$RuCl_3$, where the angle is defined between the external magnetic field and the ab-plane of α-$RuCl_3$. The Majorana fermions in a spin liquid state are expected to have a great impact on research of strongly correlated quantum matter, opening up the possibility of topological quantum computing. Kitaev gave the exact solution of the honeycomb model named after him, by means of introducing the Majorana operator, which implies that a spin-liquid state is the ground state in this model. After his theoretical proposal, heavy transition metal insulators with d^5 electronic configurations renewed people's interest because of the potential realization of quantum spin liquid state. Various Kitaev-candidate materials like the 2D honeycomb Na_2IrO_3 and α-$RuCl_3$ have been studied experimentally. Those experimental studies have proved that the presence of additional anisotropic interactions beyond the Kitaev coupling induce a variety of magnetic orders in these systems at zero magnetic field, spoiling the potential spin liquid. The effects of magnetic field are claimed to be a possible route towards inducing novel spin liquid phases via suppressing those trivial magnetic orders. The anisotropic interaction may come from higher order chiral spin interactions, bilinear anisotropic interactions or anisotropic g-factor. And it results in a distinct sawtooth angular dependence of the magnetic torque over a wide range of magnetic fields. Very recently, K. Riedl et al. [Phys.Rev.Lett.**122**,197202 (2019)] reported that anisotropic interactions or the anisotropic g-factor is sufficient to explain the angular dependence, i.e. the anisotropic property in α-$RuCl_3$, which is still necessary to be verified by the experiment with an strong external field. We measured the magnetic field -angle phase diagram of α-$RuCl_3$, and verified the validity of the theory of K. Riedl et al. I believe further theoretical study of spin liquid states based on the K. Riedl et al.'s Hamiltonian model will lead us to better understanding of the field-induced spin liquid in α-$RuCl_3$.

In the third work, I focus my attention to electric properties of the Kondo insulator, YbB_{12}. I have developed a contactless magnetoresistance measurement technique to investigate the magnetic field induced phase transitions of YbB_{12} in a magnetic field of up to 120 T. Generally, the Kondo bound state results in the heavy effective mass and forms the so-called Kondo metal

(KM). However, some Kondo metal systems such as SmB_6 and YbB_{12} show insulating behavior at low temperatures. These systems are called Kondo insulator (KI). The mechanism of formation of the electrical insulating phase in the Kondo insulator at low temperatures is still not entirely clear. Recently, Terashima et al. reported a two-step metamagnetism in YbB_{12} from the magnetization process measurement up to 120 T [J. Phys. Soc. Jpn. **86**, 054710 (2017)]. The specific heat study indicates the two-step phase transitions is a Kondo insulator -Kondo metal - normal metal transition [Terashima et al., Phys. Rev. Lett. **120**, 257206 (2018)]. A direct electrical transport measurement is required to unveil the origin of the second higher-field transition that occurs at around 100 T. The Kondo metal - normal metal transition would induce a decrease of the electrical resistivity due to breaking of the Kondo bound state. On the other hand, electric resistivity measurements in the 100-T class pulse magnetic field is technically challenging. A Joule heating problem induced by Lenz's law becomes serious for the measurements especially for good metals. In the present study, I have developed a contactless magnetoresistance measurement method and observed the magnetoresistance in YbB_{12} at a low temperature up to 120 T.

Acknowledgements

First of all, I would like to thank my supervisor, Prof. Yasuhiro Matsuda. When I was a master, I focused on applied magnetic physics. At that time, I measured the magnetization by using a VSM which can only get 1 T magnetic field, so I really wanted to have a strong magnetic field to perform the experiment. So, I contacted Professor Matsuda to ask about the enrolment of PhD. I still can't believe I got a positive reply from Prof. Matsuda at that time. After I arrived in Japan, I made a lot of mistakes, and couldn't understand nearly everything about experiments. Prof. Matsuda always gives me kind suggestions once by once. It was really a wonderful experience during I stay in Matsuda group.

I want to thank Dr. Kazuya, Dr Akimoto and Dr. Matsui specially. Kazuya san and Akimoto san gave me a lot of suggestions on experiments and lives. Matsui san come to Megagauss later than me, but he training my Japanese nearly every day. Before Matsui come to Megagauss group, I always can't understand what others are discussing. This condition changed after his coming.

Ikeda san, Nomura san and Nakamura san are Research Associate in destructive group. They taught me a lot of experimental details for the last four years. Matsuo san helped me a lot in measuring the magnetization in short-pulse magnetic field. Dr. Yuan Yao taught me a lot of theoretical knowledge at last four year. Dr. Zhuo Yang told me many experimental skills. Prof. Takeyama, Prof. Kindo, and Prof. Kohama gave me many suggestions in performing the experiments.

Prof. Tanaka in Tokyo in Tokyo Institute of Technology provided me the sample $TlCuCl_3$ and α-$RuCl_3$. Prof. Iga in Ibaraki University provided me the sample YbB_{12}. Without those sample, I don's think I can graduate and get the Ph. D degree. Prof. Tokunaga, Prof. Kato, Prof Kimura, and Hosono Sensei be responsible for My Ph. D thesis. Thank you very much.

I also want to thank other members in Megagauss group.

At last, I would like to thank my wife Hong Ye for silent supporting on my study.

Contents

Chapter 1

Introduction

Magnetism is one of the basic properties of matter in real life. Magnets have similar properties, such as attraction to some magnetic objects, because they are made up of atoms, some or all of which are themselves tiny magnets. When all or most of the atomic magnets are aligned in the same direction, they produce an observed effect, so the net effect is the sum of all the individual magnets and is therefore macroscopic. In order for these atomic magnets to align, there must be a force between them. One possibility of such forces is a normal magnetic dipole interaction, which can produce a tendency for the two magnetic dipoles to be either parallel or antiparallel, or actually arranged at any angle, depending on their relative positions. This is a long scale interaction across many atomic spaces. But magnetic dipole interactions are too weak to explain room-temperature magnetism. If this were the only possible interaction, macromagnetism would occur only at very low temperatures, where thermal fluctuations are too weak to disrupt the good order.

In fact, interactions practical atomic magnets for magnetic materials are arranged by exchange. This is a direct result of Pauli's exclusion principle, which is basically due to the electricity between the electrons in the atom, rather than to the magnetic force. Since forces are much stronger at the atomic scale than magnetic forces, this explains why the exchange interactions are so strong that they can produce magnetism at a macroscopic scale, even at room temperature. The form of the exchange interaction is much simpler than that of magnetic dipole interaction. In addition, it produces a short-range effect and depends on the overlap of the atomic wave functions.These two facts make it easier to deal with than magnetic dipole interactions.

Those exchange interactions can be divided into direct and indirect interaction. In an insulator, electrons are usually localized at a fixed lattices site. The spin of the electron interacts with the spin of the surrounding electron from the direct or indirect interaction. They are usually described by the following Hamiltonian,

$$\mathcal{H} = J \sum_{\mathbf{i},\mathbf{j}} \mathbf{S_i} \cdot \mathbf{S_j}, \tag{1.1}$$

here, J represents the interaction parameter. It is determined by the form of exchange. For example, superexchange interaction often gives a positive exchange parameter, which makes the energy of two adjacent spins aligned in opposite directions lower. As we mentioned earlier, it originates from the Coulomb interaction. When dealing with specific problems, this exchange effect is often regarded as a constant, rather than a complicated many-body Coulomb interaction problem. Thus, this description is actually an approximation of the interaction from electricity force to spin interaction. Although the localized spin Hamiltonian is only an approximate model of the Coulomb interaction, it still provides us with a wealth of physical conclusions. With the development of condensed matter physics experiments, more and more experimental phenomena prove that this approximation is very effective. Recent research on magnon dynamics, spin liquid and other issues has aroused widespread interest in localized spin models.

In metals, electrons tend not to be localized, but to be itinerant through the metal lattice as conducting particles. In this case, the localized Hamiltonian fails. A localized magnetic moment polarizes the spins of conduction electrons and this polarization in turn couples to a neighbouring localized magnetic moment a distance r away. The exchange interaction is thus indirect because it does not involve direct coupling between magnetic moments. It is known as the RKKY interaction (or also as itinerant exchange). The name RKKY is used because of the initial letters of the surnames of the discoverers of the effect, Ruderman, Kittel, Kasuya and Yosida. Kondo effect is a famous phenomenon in the metal. In very dilute alloys of magnetic ions in a non-magnetic host, the magnetic moments of the magnetic ions can be considered as independent if we ignore the RKKY coupling. The only remaining interaction is between the magnetic moment and the conduction electron spins. At high temperatures the magnetic moments behave like free, paramagnetic moments but below a characteristic temperature, known as the Kondo temperature T_K, the interaction between the magnetic moment and the conduction electrons makes the impurity spin non-magnetic. What is happening is that the conduction electrons begin to form a cloud of opposite spin-polarization around the impurity spin resulting in a quasi-bound state. This process of magnetic screening of a magnetic impurity by the conduction electrons is known as the Kondo effect.

I will present my research on the interactions of spins in insulators and metals. Intriguing phenomena such as including Bose-Einstein condensates of magnons, Majorana spin liquids, and collapse of the Kondo band state.

Chapter 2

Background of correlated spin systems

In this chapter, I introduce the background of correlated spin system, and the importance of ultrahigh magnetic fields in the study of these problems.

Insulators can be classified by the origin of their gaps, such as band insulators, Mott insulators, Kondo insulators, and others. In band insulators, or some Mott insulators which the charge effect is insignificant, the spins become independent with the charged gap, localized at the lattices, and affect the magnetism of the system by interacting with the surrounding spins. These systems are called quantum spin systems (QSS) when the quantum effects are significant. The theory of QSS was developed by Heisenberg after the discovery that the electrons have an intrinsic angular momentum experimentally. As the basic models of quantum magnetic insulators, QSS are relevant to almost the whole host of magnetic materials. In some low dimensional systems (1,2-dimensional system), those theories are particularly fruitful because their simplicity has enabled exact solutions to be found but they still contain many highly non-trivial features. Furthermore, there are also many cases, for example 3-dimensional spin systems, in which we can find no exact solution. In these cases, they can be used as a prototype system for developing approximate methods of modern quantum mechanics.

QSS can be divided into two categories: the non-frustrated system and the frustrated system respectively. Frustrated or not is a classification method of spin system, which corresponds to the localized and itinerant magnons respectively. The most classical example is the antiferromagnetic Iising model which only considers the nearest neighbor model. On the triangular lattice, the interactions between adjacent bands conflict with each other, leading to a frustrated system which the ground state is degenerated. And those phenomenon doesn't happen on the square lattice with only nearest interaction, which we called it non-frustrated system. Under external magnetic field, the frustrated spin systems give some magnetization plateaus. Those plateaus was understood as a superfluid-insulator transition of hard-core-bosons, which correspond to the triplet polarized along the external field. The stabilization of plateaus is because of the quantum fluctuations, or the suppressed kinetic energy in coupled-dimer systems by frustration. Non-frustrated spin systems do not give those magnetization plateaus, but a continuous magnetization until saturation. Bose-Einstein condensation is a famous case in non-frustrated 3-dimensional systems. In this thesis, Bose Einstein condensate (BEC) of magnons in three dimensional systems and the spin liquid in two dimensional systems are studied as the first and second topics. They are the subject of non-frustrated and frustrated spin system, respectively. The background of BEC studies are introduced in Sec. 2.1, the background of spin liquid studies are introduced in Sec. 2.2.

In other types of insulators, the charged gap is related to the electron-electron interactions, which should studied by a strong correlated picture. Kondo insulators is one example of them. The spin of the 4f electron contributes to the formation of the charged gap. The charged gap is thought to be from the strong coupling between 4f electrons and conduction electrons. i. e. Kondo effect. Those systems are insulator at low temperature, and translates in to Kondo metal and normal metal state as temperature increase. The study of Kondo insulators provide a chance to understand the many body problem deeply in condensate matters, especially after the topological Kondo insulator concept was proposed. However, the number of Kondo insulator is rather limited until now. The famous examples are SmB_6, YbB_{12} and $Ce_3Bi_4Pt_3$. In this thesis, the behavior of Kondo insulator YbB_{12} under external field are investigated as the third topic. The background of Kondo effect and Kondo insulator are introduced in Sec. 2.3.

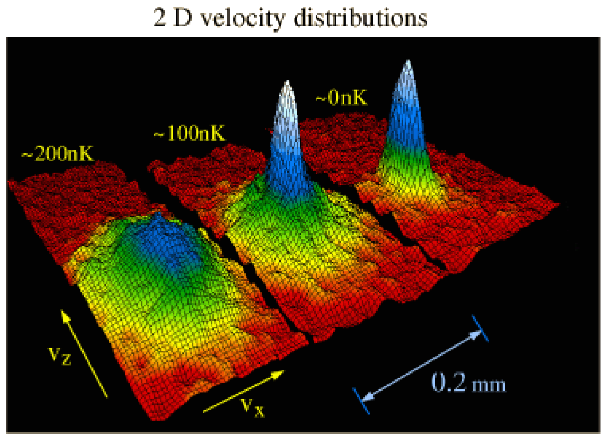

Figure 2.1: BEC of cold atoms [1].

2.1 BEC of magnons in non-frustrated gapped spin dimer system

Bose-Einstein condensation (BEC) is one of the most fascinating purely quantum-mechanical phenomena. Early experiments had successfully realized the BEC state on dilute atomic gas system under nanokelvin temperatures with the laser cooling technique [1], as shown in Fig. 2.1. The fact that nanokelvin temperatures is required makes experimental studies of BEC difficult to conduct and the number of the researches is limited.

On the other hand, based on a correspondence between a quantum antiferromagnet and a lattice Bose gas system [2], the new research area on BEC with spin (s) systems in which spins are strongly correlated to each other, has been opened up in recent two decades. It has been proposed that the field-induced ordering phase in $TlCuCl_3$ (a three-dimensional s=1/2 spin-gap dimer system) can be interpreted as a BEC phase of magnons [3–7], as shown in Fig. 2.2 and its magnetic field-temperature (H-T) phase boundary is claimed to follow the power-law dependence as,

$$g|H_{c1}(T) - H_g| \propto T^{\alpha}, \tag{2.1}$$

where g is the g-factor of the spin system, H_{c1} is one of the critical magnetic fields of the BEC at a finite temperature T, H_g is the critical magnetic field at zero kelvin, and the critical exponent $\alpha = 1.5$ under Hartree-Fock-Popov (HFP) approximation. The experimental phase boundary is shown in Fig. 2.3. It also provides a new experimental approach to study the BEC, i.e., magnons in three-dimensional spin-gap dimer system are studied as bosons in a lattice system.

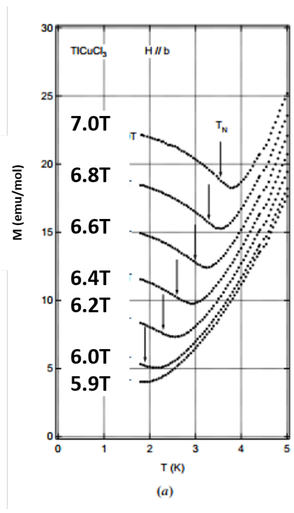

Figure 2.2: Field-induced ordering phase in $TlCuCl_3$ [3].

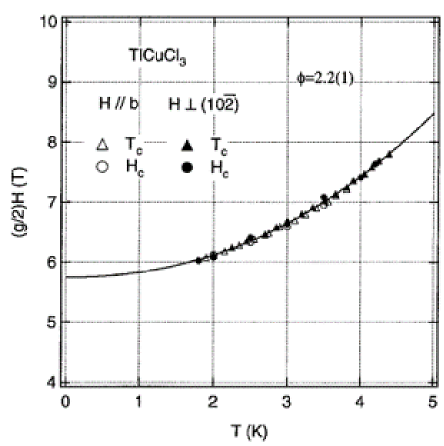

Figure 2.3: Phase boundary of $TlCuCl_3$ [3].

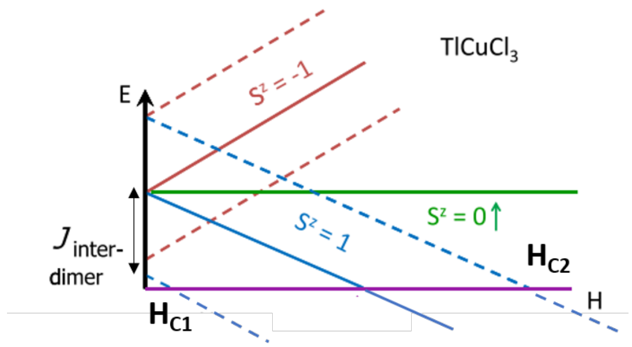

Figure 2.4: Zeeman image of spin dimer system

In contrast to the ultra-cooling atomic gas, observations of critical behaviors around quantum critical points in the spin systems are accessible because of their high degree of homogeneity in boson density and wide temperature window of the critical boundary [8]. In a pure dimer system, the transition between singlet state and the $S_z = 1$-triplet state under an external magnetic field drives a phase transition at the critical magnetic field $H_g \equiv \Delta/g\mu_{\rm B}$ with Δ the spin gap. The H_g separates into two distinct critical points H_{c1} and H_{c2} in real spin-gap materials due to inter-dimer interactions; these two critical magnetic fields correspond to the begining and saturation of the magnetization, respectively, as shown in Fig. 2.4. The criticality in the vicinity of the H_{c1} along the H-T phase boundary has been extensively studied in several materials such as $\mathrm{TlCuCl_3}$, $\mathrm{Ba_3Cr_2O_8}$ and $\mathrm{Sr_3Cr_2O_8}$, by means of magnetization, magnetostriction, neutron and magnetocaloric effect (MCE) measurements [9–14]. The whole phase diagrams of most gaped spin dimer systems are also given by those measurement method [13, 14]. On the other hand, detailed experimental measurements at the high-field side near H_{c2} are still lacking for materials that possess large H_{c2} like $\mathrm{TlCuCl_3}$. Based on the prediction of bond operator theory, H_{c2} of $\mathrm{TlCuCl_3}$ is about 80 T [15], which is a challenge measurement in experiment because of the ultrahigh magnetic field is necessary. In this study, our purpose is to clarify the BEC behavior in the vicinity of the H_{c2} in $\mathrm{TlCuCl_3}$ by employing the single turn coil technique.

2.2 Frustrated spin system and spin liquid state

In traditional magnetic materials, spin interactions result in phase transitions from a high temperature disorder state to a magnetic ordered state as temperature decreases. This transition is usually accompanied by thermodynamical singularities observed at the transition point due to a spontaneous symmetry breaking. An entropy drop to zero happens when the system enters an ordering ground state. However, by forming a collective quantum spin state with long range quantum entanglement, the spin entropy can also be released at zero temperature without any symmetry breaking. This kind of state of matter is called quantum spin liquid (QSL) [16, 17]. One of the goals of condensed matter physics is to find new quantum phases formed from interacting spins and electrons. And thus, the QSL is probably one of the most interesting quantum phases ever known.

The study of spin liquids was initiated by Anderson in 1973 by his conjecture about the resonant valence bond (RVB) state [18]. When Heisenberg's spin with the antiferromagnetic interaction and a $S = 1/2$ spin moment is placed on a triangular lattice, the interaction on the different bonds is limited by the geometry; At first glance, this should prevent the spin from finding a unique way to break the symmetry. Anderson pointed out that the ground state of the system consists of the spin quantum superposition of the singlet state to form a double $S = 1/2$ spin, a pair of rotating wave liquid in a manner similar to the ordered state of the ground magnetic field. This model gives an intuitive picture of the QSL state. However, the ground state of the $S = 1/2$ Heisenberg antiferromagnet on a triangular lattice was soon proved to be ordered: the non-collinear 120° structure, RVB-QSLs are also thought to exist in other frustrated lattices, such as Kagome lattices or triangular lattices with additional interactions [19].

One feature of RVB-QSLs is the unusual fundamental excitation described by a moving fermion $S = 1/2$ quasiparticle (called Spinons), as in the case of one-dimensional $S = 1/2$ Heisenberg antiferromagnetism. The excitation value of a conventional magnet is $S = 1$ and usually appears in the form of a peak value in the scattering experiment. For a given momentum, the peak energy is sharp, i.e., a magnon with a definite dispersion. In RVB-QSLs, the traditional $S = 1$ excited fractional results in spinon pairs. The spin produces an excited energy continuum at a given moment, much like electron excitation in a metal. The spin produces an excited energy continuum at a given moment, much like electron excitation in a metal [20, 21].

The RVB-QSL-like behavior has been observed in some triangular and kagome lattices, like $ZnCu_3(OH)_6Cl_2$ [22]. In those material, the magnetic order is absent even down to the lowest temperature which can be measured experimentally. It is at least two orders of magnitude smaller than the energy scale of magnetic interaction. In $ZnCu_3(OH)_6Cl_2$, the continuum excitations with a small excitation gap was also observed by using inelastic neutron scattering and NMR measurements [22]. Those results hint the fractionalized excitations are expected for a QSL.

Although the research of RVB-QSL has made remarkable progress, the difficulty lies in that the exact solution has never been obtained in real model Hamiltonian. Alexei Kitaev presents a simple new model [23], named by after him. The Kitaev model consists of S = 1/2 spin on a honeycomb lattice, interacting with a simple bond-dependent axis parallel to the X, Y, or Z axis in its nearest neighbor site's spin (Figure 2.5). The Hamiltonian of Kitaev model is

$$\mathcal{H} = -\sum_{\langle \mathbf{i},\mathbf{j}\rangle_\gamma} K_\gamma S_{\mathbf{i}}^{\gamma} \cdot S_{\mathbf{j}}^{\gamma}, \tag{2.2}$$

where $\langle$i, j$\rangle$ is a $\gamma = x$-type, y-type or z-type bond and the summation is taken over all honeycomb bonds. This model is fully solvable, and gives the QSL ground state, where the spin is divided into the quasi-particle, Majorana Fermions, as shown in figure 2.5. Kitaev's work provided a new chance in investigating the QSL state in honeycomb lattices.

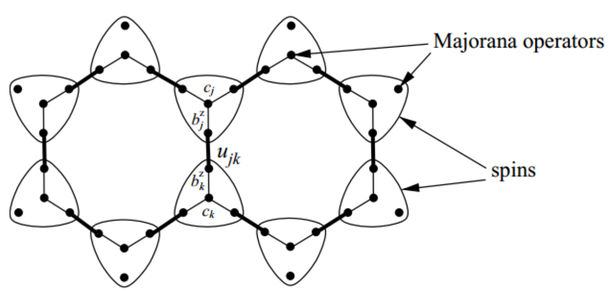

Figure 2.5: Graphic representation of Hamiltonian, from Ref. [23]

The Kitaev model was thought to be a toy model at first, because of the pure S = 1/2 spin does not normally accommodate strong anisotropy. However, due to the interaction between correlation and strong spin orbital coupling, heavy 4d and 5d transition metal compounds which exhibit associated electron physics have become possible way to realize the Kitaev behavior. Kitaev QSL's potential hosts are Ir^{4+} oxide and Ru^{3+} chloride, with a d^5 electron configuration and rock-salt-related honeycomb structure.

In real materials, S = 1/2 model are realized by a lager crystal field of the octahedral. In the Ir^{4+} oxide of the octahedral coordination of oxygen ions, the oxygen octahedron produces a large crystal field splitting of 3 or 4 eV. This splitting wins the Hund's first law in favor of a high spin state and suppresses all of five electrons localized in the triply degenerate t_{2g} manifold that comprises d_{xy}, d_{yz} and d_{zx} orbitals, as shown in Fig. 2.6. The five localized t_{2g} electrons form a six-fold degenerate state made of total spin moment $S = 1/2$.

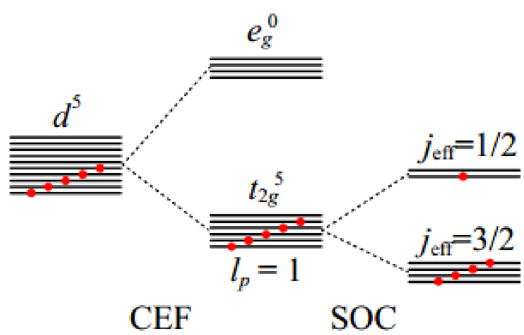

Figure 2.6: Crystal field effect on condidate material [24, 25]

In addition, in order to satisfy the K-exchange interaction term in Kitaev model, strong spin orbit coupling and corresponding crystal structure are very important. Here, we skip the discussion of implementing K-exchange interactions, although they are very interesting because I am not focused on the design of material to realize the Kitaev model. It is necessary to note that, although the geometrical structure and spin coupling characteristics of Kitaev candidate materials provide the conditions for the implementation of the Kitaev K-exchange interaction term, some other non-Kitaev interactions always result in an ordering ground state of the system at low temperature. With the change of the exchange interaction parameters of these non-Kitaev terms, the ground state of the system may show ferromagnetism, Neel, Zigzag, Stripy and pure spin liquid. Theoretical studies related to the Heisenberg-Kitaev model [26] give the ψ dependent ground state phase diagram, where ψ is a parameter of exchange interaction from $\mathcal{H} = A[\sum_{\langle \mathbf{i},\mathbf{j}\rangle_\gamma} 2sin\psi S_{\mathbf{i}}^{\gamma} \cdot S_{\mathbf{j}}^{\gamma} + cos\psi \mathbf{S_i} \cdot \mathbf{S_j}]$, as shown in Figure 2.7.

With the efforts of scientists engaged in crystal synthesis, several candidate materials have been proposed to realize Kitaev model, including A_2IrO_3 (A = Na, Li), α-$RuCl_3$ and so on. One problem is no candidate materials show pure Kitaev spin liquid state in the ground state up to now. Therefore, studying the phase diagram of these candidate materials under the temperature and external magnetic field has become an important topic. Figure 2.8 shows the possible temperature- and magnetic-field-dependent phase diagram of the candidate materials [25]. One hopes to find a candidate system which is located at the Dashed line's location. In such a system, the ordered state of the system is gradually destroyed or suppressed with increasing temperature or magnetic field, thus entering a spin liquid state dominated by the Majorana fermions possibility. At higher temperatures or magnetic fields, the system gradually becomes a free system. Meanwhile, in order to describe the real model of these actual candidate materials, Heisenberg-Kitaev model, J-K-Γ model and so on have been introduced successively [26]. Specially, the J-K-Γ model has attracted the most attention from experimental subjects. the J-K-Γ model is shown as fellows,

$$\mathcal{H} = \sum_{\langle \mathbf{i},\mathbf{j}\rangle} J\mathbf{S_i} \cdot \mathbf{S_j} + K_\gamma S_{\mathbf{i}}^{\gamma} \cdot S_{\mathbf{j}}^{\gamma} + \Gamma(S_{\mathbf{i}}^{\alpha} \cdot S_{\mathbf{j}}^{\beta} + S_{\mathbf{i}}^{\beta} \cdot S_{\mathbf{j}}^{\alpha}), \tag{2.3}$$

where i, j is the nearest sites, α and $\beta = x$, y and z with a cyclic ordering. Among the many candidate materials, ruthenium trichloride has a unique advantage due to its octahedral structure being less distorted than yttrium oxide [24]. Therefore, two problems become interesting. The first one is that the measurement of α-$RuCl_3$ under magnetic field are expected, which is possible to realize the spin liquid state. The second one is the parameters of J-K-Γ model is possible confirmed by the measurement under magnetic field. Based on the experimental results in Ref. [27, 28], the saturation magnetic field of α-$RuCl_3$ is higher than 70 T for external field perpendicular with the ab-plane. It is meaningful to measure the magnetization process by employing the single-turn coil technique, which can give us a magnetic field up to 100 T.

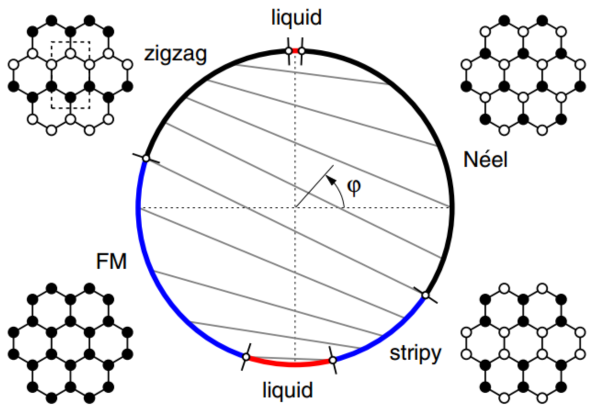

Figure 2.7: Possible ground state of condidate materials, from Ref. [26]

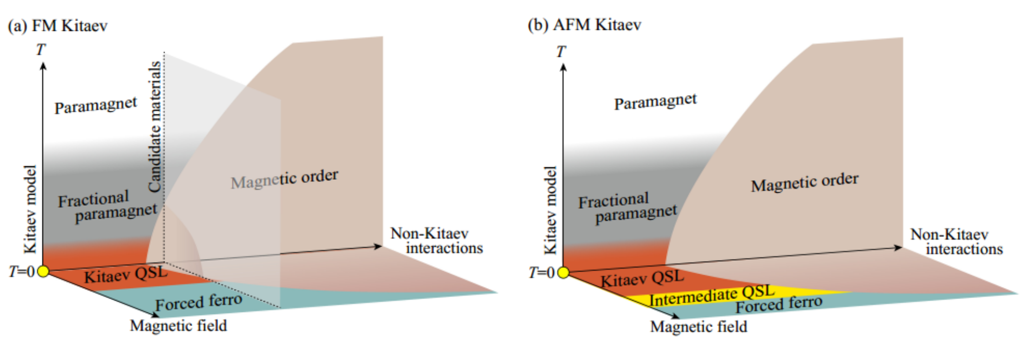

Figure 2.8: Schematic phase diagrams while changing temperature T, magnetic field, and non-Kitaev interactions [25].

2.3 Kondo effect and Kondo insulator

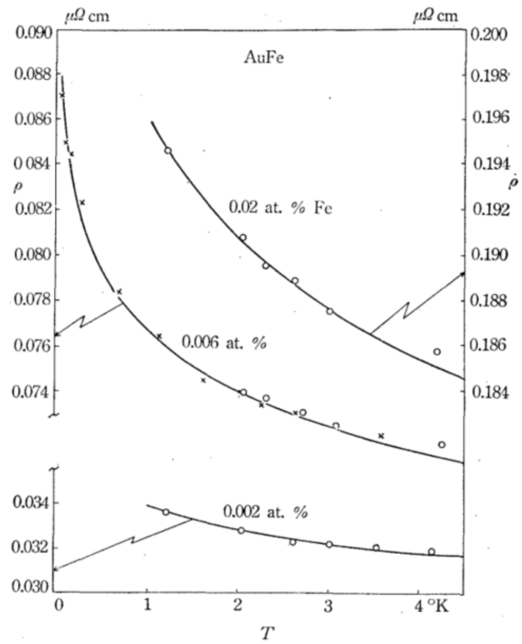

Figure 2.9: Comparison of experimental and theoretical ρ-T curves for dilute AuFe alloys [29].

The Kondo effect is pointed out by Jun Kondo [29] to explain the resistance minimum problem, which was observed in dilute magnetic alloys, like Cu, Ag, Au, Mg, Zn with Ce, Mn Fe, Mo, Re, Os as impurities. He studied this dilute magnetic effect by employing the perturbation theory, as shown bellow.

$$\mathcal{H}_0 = \sum_{\mathbf{k}s} \epsilon_{\mathbf{k}} \alpha^{\dagger}_{\mathbf{k}s} \alpha_{\mathbf{k}s}, \tag{2.4}$$

$$\begin{aligned} \mathcal{H}' &= \sum_{n\mathbf{k}\mathbf{k}'} \exp[i(\mathbf{k}-\mathbf{k}')\cdot\mathbf{R}_n] \times [(\alpha^{\dagger}_{\mathbf{k}',+}\alpha_{\mathbf{k},+} - \alpha^{\dagger}_{\mathbf{k}',-}\alpha_{\mathbf{k},-})]S_{nz} \\ &+ \alpha^{\dagger}_{\mathbf{k}',+}\alpha_{\mathbf{k},-}S_{n-} + \alpha^{\dagger}_{\mathbf{k}',-}\alpha_{\mathbf{k},+}S_{n+}, \end{aligned} \tag{2.5}$$

where $\mathcal{H}_0$ denoting the kinetic energy of conduction electron, $\mathcal{H}'$ denoting the correlation between magnetic impurities and conduction electrons. s is the component of the spin along the z-direction. n denotes the position vector of the n-th impurity atom. As a result, the temperature dependence of resistance due to the Kondo effect is $\rho_{spin} = A - B \cdot logT$, where A and B are constants that depend on the systems. After considering the lattice scattering and impurity potential, the resistance is summarized as

$$R \;=\; a\, T^5 + b\, \rho_0 - c\, logT, \tag{2.6}$$

This results successfully explained the minimum resistance in dilute magnetic alloys, as shown in figure 2.9. After Kondo's theory was proposed, the interaction between localized spins and conducted electrons in enriched magnetic impurities systems become an interesting topic in solid state physics. Those systems are typical many-body system due to the enriched magnetic impurities. A large variety of physical phenomena, like spin glass, cluster glass, and heavy Fermi liquid, are studied in those systems experimentally.

Theoretically, P.W. Anderson [30] proposed a sample model to describe the effects of correlations for d-electrons in transition metals, which is called periodic Anderson model (PAM). This model consists of three terms, which is to describe the uncorrelated conduction electrons, correlated electrons, and the hybridization between correlated and uncorrelated electrons, respectively. The Hamiltonian expression is

$$\begin{aligned}
\mathcal{H} &= \mathcal{H}_c + \mathcal{H}_f + \mathcal{H}_{cf}, \\
\mathcal{H}_c &= \sum_{i,j,\sigma} t_{ij} c^\dagger_{i\sigma} c_{j\sigma}, \\
\mathcal{H}_f &= \epsilon_f \sum_{i\sigma} f^\dagger_{i\sigma} f_{i\sigma} + U \sum_{i} f^\dagger_{i\uparrow} f_{i\downarrow}, \\
\mathcal{H}_{cf} &= \sum_{i,j,\sigma} V (c^\dagger_{i\sigma} f_{i\sigma} + h.c.),
\end{aligned} \tag{2.7}$$

Although this model cannot be exactly solved in general, by combining with the approximate method, such as dynamical mean field theory (DMFT), it has been proved to work well in describing the behaviours of heavy Fermi liquid systems. A famous example is the discussion on the Kadowaki-Woods relationship based on PAM framework [31, 32].

Under the framework of PAM, many Kondo-class systems have so far been understood well. However, a special case is the Kondo insulator, or alternately as heavy-fermion semiconductors. A partial list of material have been assigned to this class, for example SmB_6 [33], $Ce_3Bi_4Pt_3$ [34], CeNiSn [35], and YbB_{12} [36]. The properties of them is they possess small gaps of the order of 1-100 meV in spin and charge excitation. The charged gap can be understood by the Kondo effect under the framework of PAM, but origin of it is still not very clear due to the existence of large many-body renormalizations.

In order to understand the Kondo insulator more and more, the observation of magnetic field-temperature (B-T) or pressure-temperature (P-T) phase-diagram of those systems have been extensively studied and they are also important as a general research topic on strong correlated electron systems. T. Ohashi et al. [37] reported a theoretical B-T phase diagram by combining the DMRG and quantum Monte Carlo (QMC) method, based on the PAM, Eq. 2.7. The results are shown in figure 2.10.

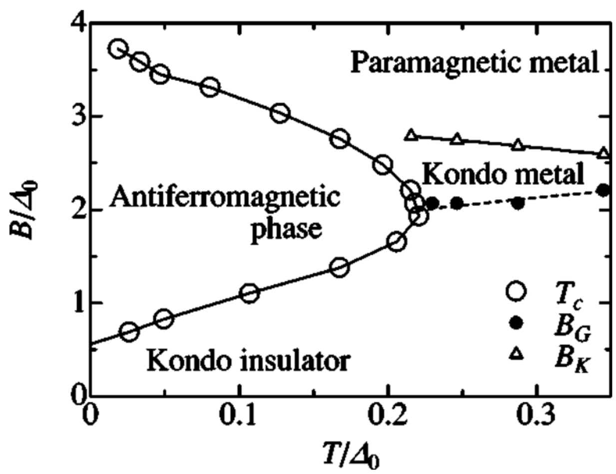

Figure 2.10: Calculated phase diagram by DMRG and QMC under PAM framework [37].

Focusing on the high temperature region ($T/\Delta > 0.22$), the Kondo insulator undergoes the Kondo insulator state (KIS), Kondo metal state (KMS), and paramagnetic metal state (PMS) as magnetic field increases. In some Kondo insulator systems, like YbB_{12}, a similar two-steps phase transition has been also confirmed by Terashima et. al. [38] by the measurement of magnetization up to 120 T. A specific heat study indicates the two-step phase transitions is a KIS-KMS-NMS transition under external field, which is necessary to be confirmed by a magnetoresistance measurement under magnetic fields. However, the joule heating problem induced by Lenz's law limited the measurement of bulk metal in the 100-T class pulse magnetic field experiment. In the present study, I have successfully observed the magnetic field dependence of electric resistance in YbB_{12} up to 120 T. I employed the single-turn coil field generator and a newly developed electric resistivity measurement technique for powdered sample. The electric property changes during the two-steps phase transitions have been revealed.

Chapter 3

Magnetic field and measurement technique

Generation of magnetic field and measurement of physical properties under magnetic fields are very important for the condensed matter physics. With the development of technology and the wide demand of scientific research, more and more magnetic field generation and measurement technology of physical properties under magnetic field have been developed. In this chapter, I will introduce various magnetic field generation methods and corresponding measurement techniques.

3.1 The method for generator of magnetic field

Artificial magnetic field can be divided into static magnetic field and pulsed magnetic field. Static magnetic fields tend to be composed of superconducting coils or large water-cooled coils, which provide a stable measuring environment, but the upper limit of the magnetic field is limmited to 45 T. The pulsed magnetic field uses LC circuit to provide a very short pulse current, and then produces a very sharp and strong magnetic field. The current indoor record of the pulsed magnetic field is 1200 T. However, in the pulsed magnetic field, the accuracy of measurement is greatly limited. Therefore, the development of measurement techniques is an important subject in pulsed magnetic field.

3.1.1 Static magnetic field generator

Using superconducting coil is a common method to realize static magnetic field. Superconducting coil magnets made of the first type of superconductor usually provide a magnetic field of up to 20 T. Such superconducting magnets are commercially available. For example, PPMS and MPMS manufactured by quantum design can provide a stable magnetic field of up to 16 T.

Bitter magnets are constructed of circular conducting metal plates and insulating spacers stacked in a helical configuration, rather than coils of wire. The current flows in a helical path through the plates. This design was invented in 1933 by American physicist, Francis Bitter. In his honor, the plates are known as Bitter plates. The purpose of the stacked plate design is to withstand the enormous outward mechanical pressure produced by Lorentz forces due to the magnetic field acting on the moving electric charges in the plate, which increase with the square of the magnetic field strength. Additionally, water circulates through holes in the plates as a coolant, to carry away the enormous heat created in the plates due to resistive heating by the large currents flowing through them. The heat dissipation also increases with the square of the magnetic field strength.

The strongest continuous magnetic fields on the earth had been produced by Bitter magnets. As of 31 March 2014 the strongest continuous field achieved by a room temperature magnet was 37.5 T produced by a Bitter electromagnet at the Radboud University High Field Magnet Laboratory in Nijmegen, Netherlands.

The strongest continuous manmade magnetic field, 45 T, was produced by a hybrid device, consisting of a Bitter magnet inside and a superconducting magnet. The resistive magnet produces 33.5 T and the superconducting coil produces the remaining 11.5 T. This magnet requires 30 MW of power. This magnet must be kept at 1.8 K using liquid helium. The magnet takes 6 weeks to cool and thus once cooled the cooling system is run continuously. It costs $1452 per hour to run at the highest field.

Recently, it seems to be a new solution to provide a static magnetic field of around 30 T by hybridizing the type I and type II superconductors. This approach greatly reduces the cost of generating a static magnetic field.

3.1.2 Non-destructive pluse magnetic field generator

When the magnetic field exceeds 40 T, the DC magnet can no longer meet people's demand for magnetic field. As an alternative, pulse magnets can give a higher magnetic field. By limiting the magnetic field produced pulse magnets are used without destruction. The non-destructive pulsed magnetic field generator consists of energy storage capacitors and a multi-layer coil. The problem of Lorentz repulsion force and Joule heat caused by a pulsed strong magnetic field should be solved in multilayer coils.

At the Institute for Solid State Physics of the University of Tokyo, professor Kindo have developed a pulsed magnets so-called Kindo magnets. The multilayer coils are protected by a Maraging steel tube, thereby avoiding stress problems. In addition, the multilayer coils are immersed in a liquid nitrogen-filled dewar, thus solving the heating problem. There are two types of Kindo magnets. The first type of magnet is designed for a use of an energy storage capacitor with a maximum energy storage of 500 kJ and an electrostatic capacity of 2.5 mF.This type of magnet can produce a magnetic field of up to 70 T for 4 ms, which is called the short pulse magnet. The other type of magnet is designed for a uses a capacitor with a maximum energy storage of 900 kJ and an electrostatic capacity of 18 mF. It can generate a magnetic field up to 60-70 T with 36 ms long pulse time, known as a med-pulse magnet. In this study, the short pulse Kindo magnet is used to generate the magnetic field up to 40 T.

3.1.3 Single turn pulse magnetic field generator

The upper limit of non-destructive magnets is about 80 T. In actual measurements, only measurements up to 70 T can generally be achieved. When the required magnetic field is greater than this, a stronger destructive magnetic field is the only solution. The single-turn coil magnetic field generator provides a destructive strong magnetic field. As shown in Figure 3.3, the single-coil magnetic field generator is composed of a set of capacitors, an air gap switches and a single-turn coil. The thickness of a single turn coil made of copper is approximately 3 mm. When a magnetic field occurs, approximately 2-4 MA current of flows through a single-turn coil, resulting in a magnetic field of up to 100 T or more. During the magnetic field, the single-turn coil explodes due to a huge Lorentz force. Figure 3.4 shows the

[1]Kazuya Nomura; Doctor Thesis, Univ. Tokyo (2019 March)

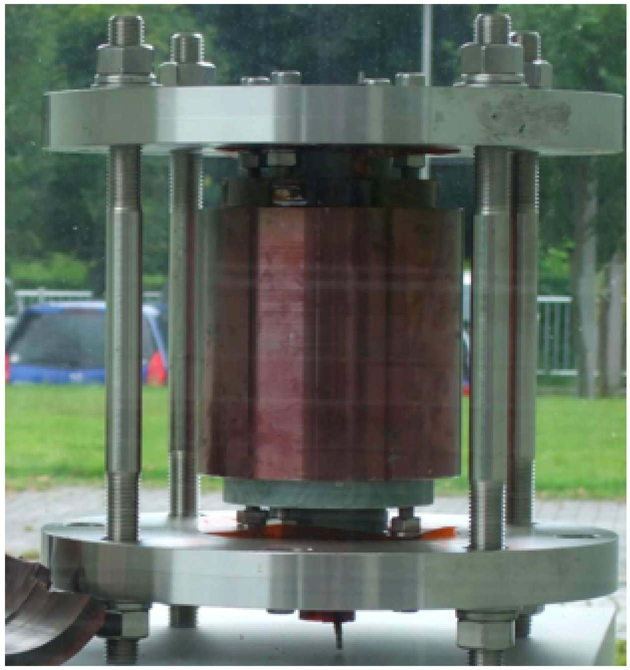

Figure 3.1: Kindo Magnet.[1]

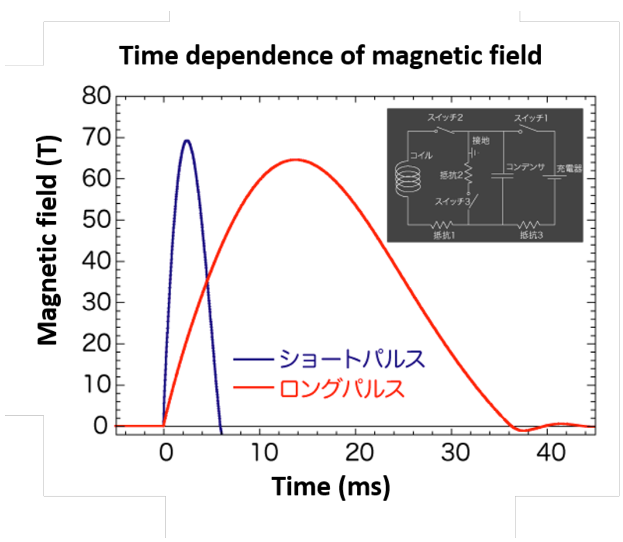

Figure 3.2: Time dependence of magnetic field generated by Kindo magnets.[1]

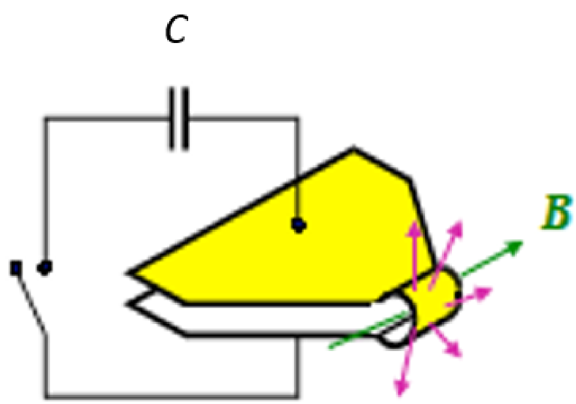

Figure 3.3: Single turn generator.

coil shape changes during the explosion. Figure 3.5 shows the comparison between before and after the coil explosion.

In the Institute for Solid State Physics, University of Tokyo, there are two destructive magnetic field generators. They are a vertical single-turn coil magnetic field generator and horizontal single-turn coil magnetic field generator, respectively. Figure 3.6 shows the time dependence of the magnetic field. In this study, a 14 mm-diameter coil and 40 kV changing voltage are often used to generate a strong magnetic field. The capacitor has a capacity of 132 uF for the vertical single-turn coil; the maximum magnetic field strength is about 102-108 T.

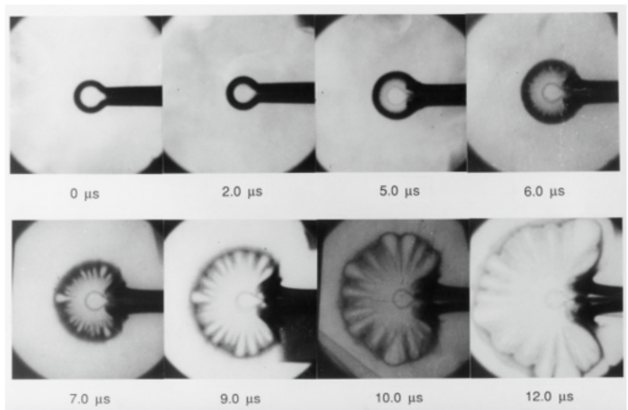

Figure 3.4: The process of explosion [39].

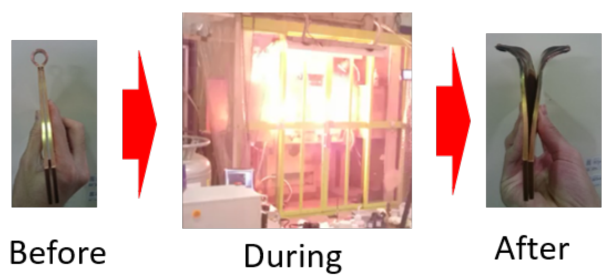

Figure 3.5: Coils before and after the explosion.

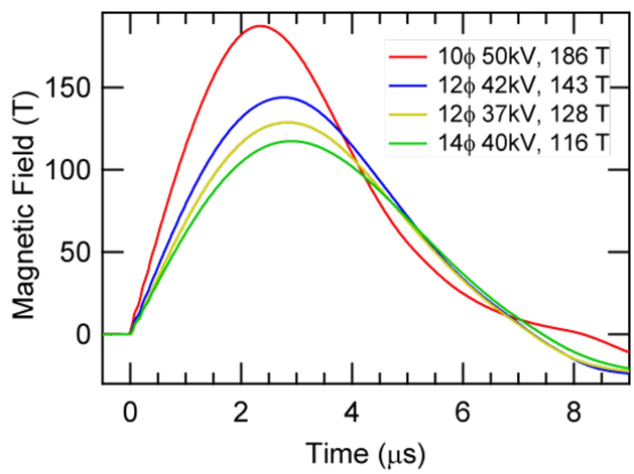

Figure 3.6: Time dependence of magnetic filed generated by Single-turn.

3.2 Development of magnetization measurement

In this study, magnetization measurement is an important experimental method. In this section, magnetization measurement methods and improvements are described in detail.

3.2.1 Magnetization measurement under a pulse magnetic field

Magnetization measurements in non-destructive magnets are made with an induction. The basic principle is the same for in the single turn coil experiment. Here, I do not describe it too much. It is worth noting that in a strong non-destructive magnetic field, the induction voltage generated in the pickup coil is small due to the longer pulse time. So what we need is to make the pickup coil turns large enough to enhance the signal of sample. Another difference between the techniques for a non-destructive and a destructive magnets is that because the induced voltage is low for the non-destructive field measurements, the insulation of the wire is not a serious problem.

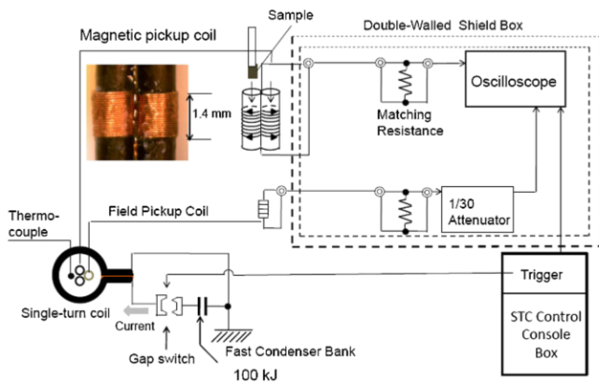

Figure 3.7: Setup of magnetization measurement [40].

3.2.2 Development of magnetization measurement under single turn field generator

In a destructive strong magnetic field, the measurement of magnetization is done by induction. Figure 3.7 shows the setup for measuring the magnetization.

Two kinds of magnetization measurement pickup coil have been developed for the single-turn coil system. They are called parallel (P)-type pickup coil and coaxial (C)-type coil, respectively. The P-type coil achieved a high level of self-compensation, and enabled us to do the precise magnetization measurements. On the other hand, The C-type coil was known to be the best for reducing the background induction component due to a magnetic field itself. Further precise measurements of both the magnetization and magnetic field are always necessary in the studies of the spin systems with spin-1/2 or spin-1. Thus, I have developed a double-layer parallel (DP)-type coil in order to improve the sensitivity of the signals.

Figure 3.8 shows the schematic figure of the DP-type coil. The basic skeleton are same with the P-type coil. The number of turns has increased from the previous 20 to 40 in each tube. One Cu-wire is used in winding the DP-type coil. Same orientations of Cu-wire between the inner-layer and outer-layer are selected when winding the wire on the tube, to avoid the difference in induced voltage, as shown in Figure 3.9. A magnetic field pick-up coil is concentrically wound around the left tube. The magnetization

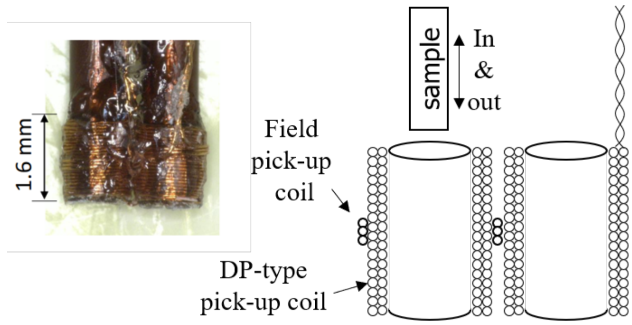

Figure 3.8: DP-type coil.

signal dM/dt is obtained by subtraction of the blank signal from the sample signal. Here, the blank signal is obtained by a measurement without the sample and the sample signal is measured with the sample. The set of two signals is obtained by two successive destructive-field measurements. This simple manner has advantages compared to the previous sample-position-exchange manner in regard to stability of the measurement position and effects from inhomogeneity of the magnetic field. The magnetization curve is obtained by a numerical integration of the measured dM/dt signal, as shown in Figure 3.10

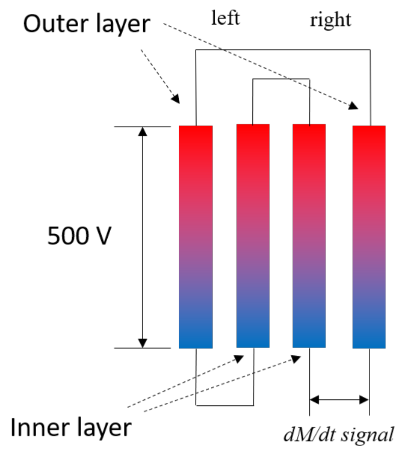

Figure 3.9: Induced voltage problem.

3.3 Development of techniques for magnetoresistance measurements

3.3.1 Magnetoresistance measurement under static magnetic field and pulse magnetic field

In the static magnetic field, the traditional measurement method is used, i.e. the four-terminal method. The advantage of this method is the accurate measurement result is obtained.

Although the four-terminal method has a strong advantage in measuring the absolute value of resistance, in strong magnetic fields, resistance is also measured by the non-contact method, such as the tunnel diode oscillator method for some special purposes.

3.3.2 Development of magnetoresistance measurement under single turn field generator

In field generated by the single-turn coil, the problem of sample heating becomes very serious because the pulse duration of the magnetic field is very short. At this point, the electrical resistance measurement of a bulk sample

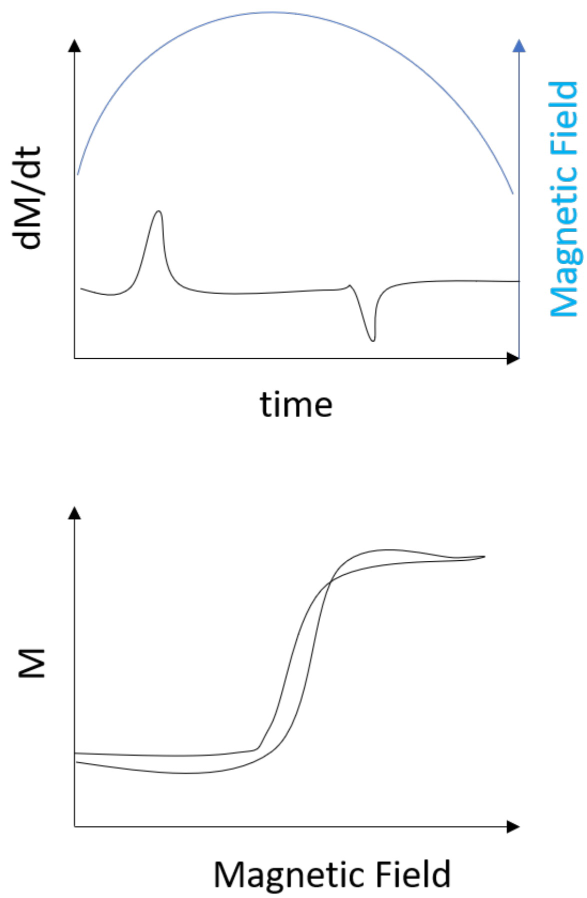

Figure 3.10: Schematic figures of calculation process of magnetization.

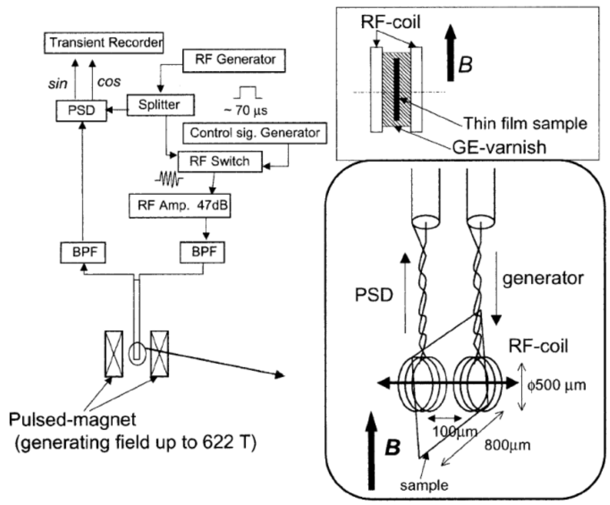

Figure 3.11: Schematic figure of high-frequency transmission method [41].

is impossible. One way to solve this problem is to use a high-frequency modulation technique. Figure 3.11 schematically shows the way to make a high-frequency transmission method. The resistivity of a sample is measured by measuring the electromagnetic transmittance of a film sample. However, it is not always available obtaining a thin-film shape sample. Therefore, measuring the resistance of powder samples is required especially for the samples that cannot be obtained as single crystals. Since induced voltage is proportional to the area of the cross section of the sample, fine powder sample can significantly the heating due to the eddy current in pulse magnetic fields.

In this study, I have used a contactless magnetoresistance measurement technique using high-frequency modulation of the input electromagnetic wave. As shown in figure 3.12, a radio-frequency generator is employed to generate a radio frequency (RF) electromagnetic wave. The powder sample is located in the RF-detect-coil and shields the RF AC field generated by the input coil. The shielding effect is picked up by the RF-detect-coil as a signal of the resistance change of the sample. This manner has advantages in measuring the electric resistance of fine powders.

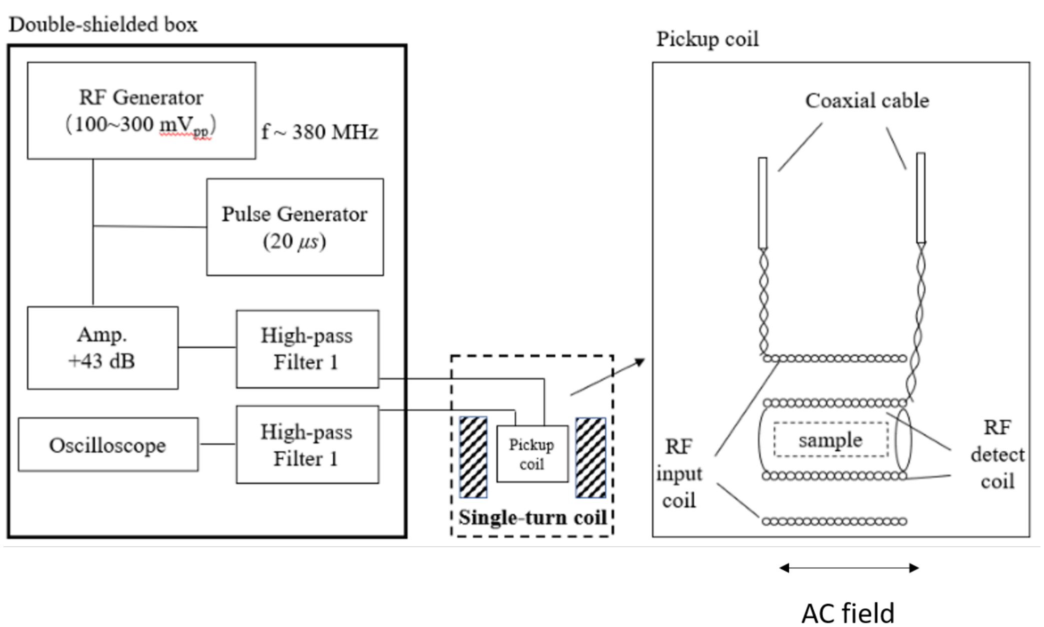

Figure 3.12: Schematic figure of high-frequency modulation method.

Chapter 4

Particle-hole symmetry breaking observed in $TlCuCl_3$ at 100 T

4.1 Particle-hole symmetry of Bose-Einstein condensation in spin dimer system

In contrast to the ultra-cooling atomic gas, observations of critical behaviors around quantum critical points in the spin systems are accessible because of their high degree of homogeneity in boson density and wide temperature window of the critical boundary [8]. In a pure dimer system, the transition between singlet state and the $S_z = 1$-triplet state under an external magnetic field drives a phase transition at the critical magnetic field $H_g \equiv \Delta/g\mu_B$ with Δ the spin gap. The H_g separates into two distinct critical points H_{c1} and H_{c2} in real spin-gap materials due to inter-dimer interactions; these two critical magnetic fields correspond to the begining and saturation of the magnetization, respectively, as shown in Fig. 2.4. The criticality in the vicinity of the H_{c1} along the H-T phase boundary has been extensively studied in several materials such as $TlCuCl_3$, $Ba_3Cr_2O_8$ and $Sr_3Cr_2O_8$, by means of magnetization, magnetostriction, neutron and magnetocaloric effect (MCE) measurements [9–14]. On the other hand, detailed experimental measurements at the high-field side near H_{c2} are still lacking for materials that possess large H_{c2} like $TlCuCl_3$.

In the theoretical analyses on H_{c2} of $BaCuSi_2O_6$ [42], the transformation from a spin Hamiltonian to an effective hard-core boson model was derived by projecting original spin states to the low-energy singlet and the $S^z = 1$-triplet states. Here, the singlet and $S^z = 1$-triplet states, respectively, correspond to the holes (particles) and particles (holes) of bosons at a low (high) magnetic field. A particle-hole symmetry [43] in this formulation is explicit in that the effective Hamiltonians at the low magnetic field and the high field are related by a particle-hole transformation on the bosonic creation operators and, thus, the magnetic-field dependence of the order parameters in phase diagrams has a symmetry with respect to the particle-hole invariant point $H = (H_{c1} + H_{c2})/2$. For instance, such a symmetry is reflected by the mirror symmetry observed in the shape of the phase boundary of the BEC phase in $BaCuSi_2O_6$. Actually, the symmetric nature is verified in the bond operator theory [44] by showing equality of the critical exponents in the vicinity of the two critical points, H_{c1} and H_{c2}. Similar symmetric phase diagram was also obtained in $Ba_3Cr_2O_8$ [13]. In the following discussion, we will call such a *phase-diagram* symmetry as "particle-hole symmetry".

It should be noted that the critical behaviors near the H_{c2} in the system of which inter-dimer interactions are strong has never been well investigated. In such systems, the particle-hole symmetry of the BEC phase boundary is expected to be broken because the conditions of the hard-core boson picture is not satisfied due to the effect of the hybridization between the singlet and $S_z = -1, 0$-triplets. According to the bond operator theory, the pressure effect (i.e. the changing of the inter-dimer interaction) on the phase boundary in the H-T plane is different at H_{c1} and H_{c2} [45], indicating that the symmetry can be modified by the inter-dimer interaction. $TlCuCl_3$ is one of the most promising materials to study the symmetry of the phase boundary and discuss the particle-hole symmetry, because it possesses strong inter-dimer interactions. H_{c1} is 5.6 T [46] and H_{c2} is theoretically predicted [15] to be about 87 T; a strong contrast of these two critical points provides us a unique situation where the degrees of the quantum hybridization between the singlet and triplet states are different between two critical points. However, H_{c2} has never been experimentally observed yet in the first-discovered magnon BEC compound, $TlCuCl_3$ because of technical difficulties to perform a 100-T class magnetic field experiment, as shown in Fig. 4.1.

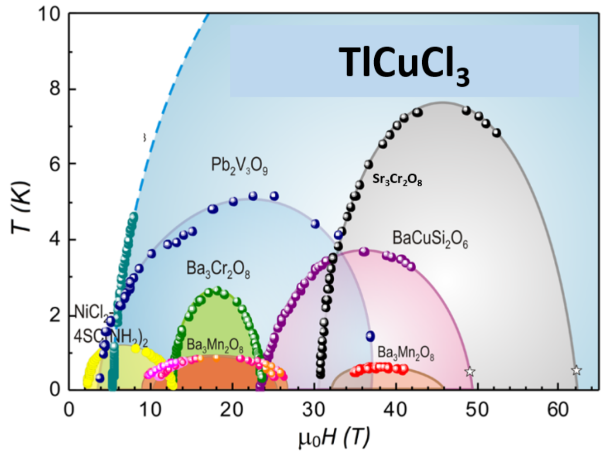

Figure 4.1: Summarized phase diagram for BEC system [47]

4.2 Magnetization process of $TlCuCl_3$

In this work, we study the magnetization (M) process of $TlCuCl_3$ up to 100 T and discuss the particle-hole symmetry breaking of the BEC phase. The particle-hole symmetry in the hard-core boson picture has been found to be broken through the quantum hybridization effect due to the strong inter-dimer interactions. H_{c2} is experimentally determined to be 86.1 T at $T \approx 2$ K that is in good agreement with the prediction by the bond-operator theory [15]. The magnetization curve (M-H curve) has a monotonous convex downward shape, which manifests the difference between the critical exponents around H_{c1} and H_{c2} and implies the absence of the particle-hole symmetry in $TlCuCl_3$. We have also precisely analyzed the M-H curve with a numerical calculation based on Quantum Monte Carlo (QMC) method. The simulation shows that the ratio of an inter-dimer interaction (J_2) and the intra-dimer interaction (J), J_2/J is about 0.35, which is consistent with the results of the neutron-scattering experiment [15]. Finally, we theoretically evaluate the critical exponents at near H_{c1} and H_{c2} and discuss on the microscopic origin of the breaking of the particle-hole symmetry using a combinatorial approach of the bond-operator theory and QMC calculation.

A single crystal of $TlCuCl_3$ [46] was used for the experiments. The $TlCuCl_3$ sample in this experiment was provided by Prof. Tanaka of Tokyo

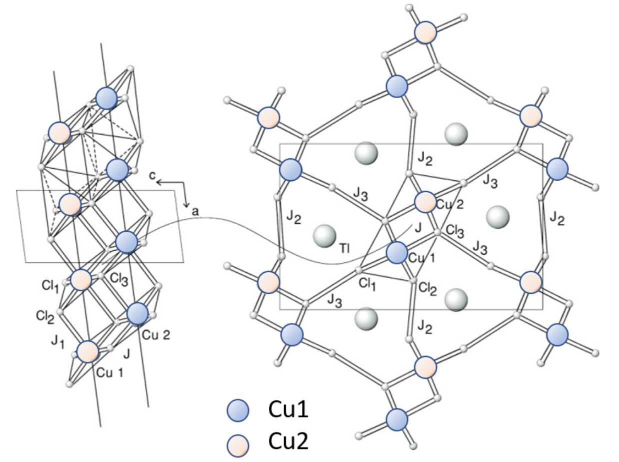

Figure 4.2: The crystal structure of $TlCuCl_3$ [45].

Institute of Technology. The crystal structure are shown in figure 4.2. The single-turn coil (STC) technique was employed to generate a pulse magnetic field of up to 110 T. The magnetization measurements have been done with a pick-up coil and an induction voltage in the magnetization process is recorded as a function of time [48, 49]. The magnetization curve is obtained by a numerical integration of the measured dM/dt signal [48, 49]. In the present work, we use a double-layer pick-up coil (the number of the turns of the coil [80 in total] is doubled from the standard number[49]) which improves the signal intensity. The details are decribed in the previous chapter. A liquid helium bath cryostat with the tail part made of plastic has been used [49], as shown in Fig 4.3, the sample was immersed in liquid helium, and a measurement temperature of 2 K was reached by reducing the vapor pressure.

Fig. 4.5 shows the magnetization process and the magnetic field dependence of the dM/dH at 2 K; The magnetization up to 60 T in Ref. [15] is also presented for the comparison of the M-H curves. The agreement of them is excellent. The M-H curve is obtained from the average of three independent experiments (Fig. 4.4) using the both up-sweep and down-sweep processes; we do not use the data of magnetization below 70 T of the down-sweep for the average because the measurement in the field-decreasing process is rather imprecise due to the field inhomogeneity [48]. We analyze the H_{c1} around 6 T using the data previously obtained with a non-destructive pulse magnet [15],

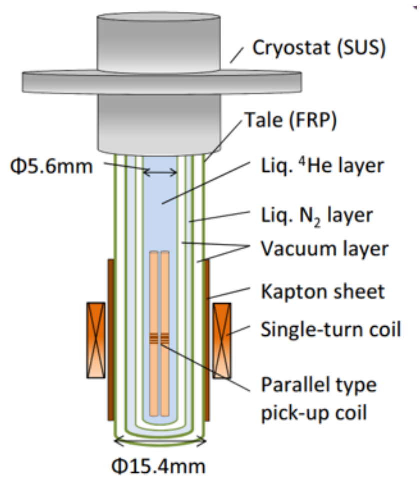

Figure 4.3: Crystat used in this study.

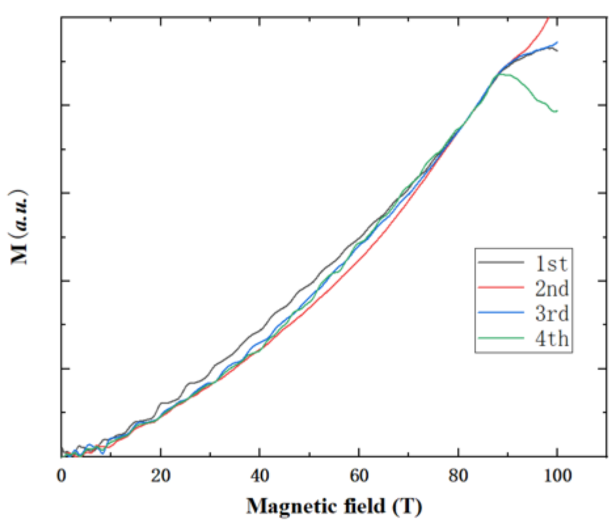

Figure 4.4: Magnetization process measured at different times

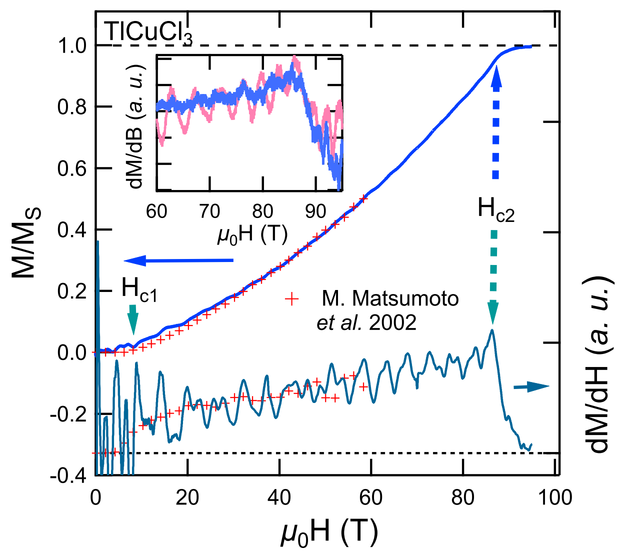

Figure 4.5: The magnetization curve measured up to 95 T, as well as the dM/dB data. Red marks represent the results of Ref. [15]. The inset shows the dM/dB data (up-sweep and down-sweep) with initial temperature at 2 K. [50]

because, at the beginning of destructive ultrahigh magnetic field generation, a huge switching electromagnetic noise is inevitably generated for injection mega-ampere driving currents [48, 49]. The magnetization is clearly measured in fields from 30 to 100 T, exhibiting the saturation at fields exceeding 90 T.

The critical behavior is observed in the vicinity of the saturation in the dM/dH curve as shown in Fig. 4.5: A clear peak labeled by H_{c2} in dM/dH curve corresponds to a kink of the M-H curve observed at near H_{c2}. The magnetization increases continuously between H_{c1} and H_{c2}, in which the M-H curve shows a convex slope.

Due to the fast sweep rate of the pulsed magnetic field ($\sim 8\ \mu$s), the sample undergoes a semi-adiabatic process. The spin entropy change caused by a phase transition is transferred into the phonons and leads to the temperature change of the sample. Therefore, it is necessary to consider the temperature change during the magnetization process. Because the MCE experiment up to 100 T is impossible to be conducted with current experimental techniques, we estimate the MCE effect using the MCE reported in another magnon BEC dimer spin system. According to Ref. [42], the temperature change at 45 T near H_{c2} in $BaCuSi_2O_6$ is around 0.03 K where the specific heat is 1.8 J/(mol K) at 2.5 K. Then entropy change ΔS=0.02 J/mol is estimated to be transferred from the magnons to phonons around phase transition point, because of the entropy change in the spins at H_{c2} should reflect the way of the saturation of the magnetization where the BEC phase is terminated. The entropy change should be of more or less a similar value as other spin systems which undergo magnon BEC with spin-1/2 dimers. Therefore, the change of entropy observed in $BaCuSi_2O_6$ can be applied to the analysis on $TlCuCl_3$. The specific heat in $TlCuCl_3$ contributed by phonons is $C_{\rm phon}$=4 J/mol K at an initial temperature $T_{\rm in}$=2 K [51], and thus the temperature rise from the initial temperature is estimated to be $\Delta S{\cdot}T_{\rm in}/C_{\rm phon}$=0.01 K for $TlCuCl_3$ at near H_{c2}. The insert of Fig. 4.5 shows $\mathrm{d}M/\mathrm{d}H$ for both field up-sweep and down-sweep processes. The overlapping of both processes implies that the temperature variation is actually small. Thus, critical points and critical exponents can be confirmed and analyzed at 2 K in the present work.

H_{c2} is determined by the peak in the dM/dH curve and found to be 86.1±0.5 T. It is very close to the predicted value obtained from the bond operator theory [15]. Furthermore, the continuous slope of the M-H curve keeps its convex shape until H_{c2}. It indicates that the critical exponents can be potentially different between H_{c1} and H_{c2} because, otherwise, it is expected that M-H curve at H_{c1} and H_{c2} should present the particle-hole symmetry behavior, i.e. the correspondences of the shapes at H_{c1} and H_{c2} are suppose to be linear versus linear, concave versus convex or convex versus concave.

4.3 Particle-hole symmetry breaking in $TlCuCl_3$

In order to interpret the observed magnetization process in more detail, we have tried to theoretically reproduce the M-H curve with a rather simple spin model. The lattice Hamiltonains in previous study are complex and include several types of inter-dimer interactions [15, 45]. Let us consider the following spin Hamiltonian to describe the universality classes around H_{c1} and H_{c2}:

$$\begin{aligned}\mathcal{H}_{\rm spin} &= J\sum_{\mathbf{i}}\mathbf{S}_{\mathbf{i},1}\cdot\mathbf{S}_{\mathbf{i},2} + J_1\sum_{\mathbf{i}}\sum_{m}\sum_{n=x,y}\mathbf{S}_{\mathbf{i},m}\cdot\mathbf{S}_{\mathbf{i}+\hat{e}_n,m}\\ &+ J_2\sum_{\mathbf{i}}\mathbf{S}_{\mathbf{i},2}\cdot\mathbf{S}_{\mathbf{i}+\hat{z},1} - g_{\|}\mu_B H\sum_{\mathbf{i},m}S^z_{\mathbf{i},m}, \qquad (4.1)\end{aligned}$$

where $\mathbf{i}$ denotes the site of dimers in a cubic lattice, $m = 1,\ 2$ shows the position of the two spins in one dimer, $\hat{e}_n = \hat{e}_{x,y,z}$ represents the unit vector. Here J denotes the intra-dimer interaction, and $J_{1,2}$ are inter-dimer interactions in different directions. We have set two different inter-dimer interactions J_1 and J_2, because it is necessary to fit and reproduce the experimental M-H curve in Fig. 4.6 and their values will be shown later. The assumed lattice for the $\mathcal{H}_{\rm spin}$ is shown in the insert of Fig. 4.6. The QMC calculation is performed using a generalized directed loop algorithm in the stochastic series expansion representation [52], as implemented in the ALPS package [53].

The calculation is performed with 10×10×10 unit cells, in which each unit cell contains two spin sites. Additionally, it has been reported that the structure of $TlCuCl_3$ is not magnetically frustrated, although the low-symmetry structure results in many triangle interaction terms in the Hamiltonian [45].

In Fig. 4.6, the magnetization curve simulated by the QMC calculation are shown with the experimental data. The simulated M-H and $\mathrm{d}M/\mathrm{d}H$ curves based on the Hamiltonian in Eq. (4.1) is represented with blue curves. The g-factor 2.23 [46] is used in this simulation. the parameters determined in this calculation are J=5.318 meV, J_1=1.074 meV and J_2=1.86 meV .

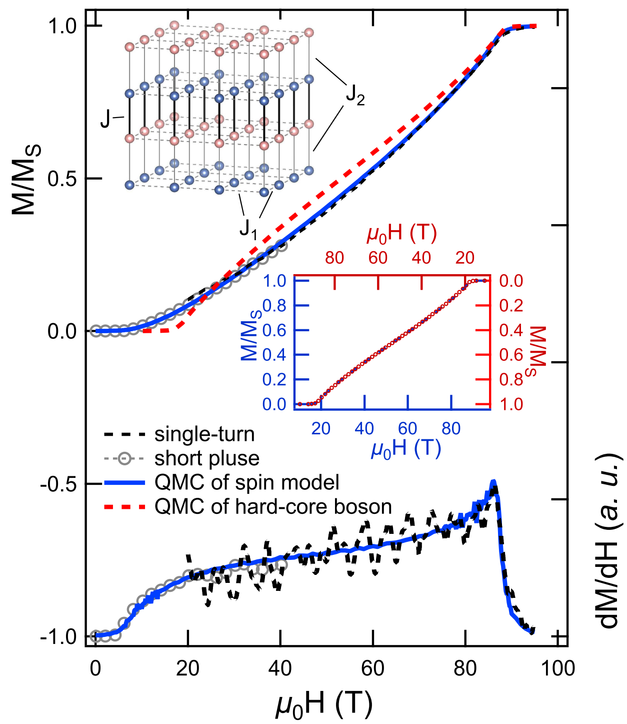

Figure 4.6: Comparison between the experimental magnetization curve and the QMC simulation results, the low field data (below 30 T) is from Ref.[15], the blue and red curves is obtained from Eq. 4.1 and Eq. 4.2, respectively. The upper inset shows the lattice of spin Hamiltonian. The red and blue ball represent the spin site 1 and 2 of a dimer in Eq. (4.1), respectively. The middle inset shows the symmetry presentation in magnetization from Eq. 4.2. [50]

In our reduced model, J and J_2 agree with those of the original model of $TlCuCl_3$ in Ref. [15, 45] according to their spin configurations. These values are also close to those reported in the previous work using the bond operator method [15]. The simulated M-H curve performed at $T = 3.5$ K is found to agree very well with the experimental magnetization process.

The hard-core boson model constructed by only the S_z=1 triplet and singlet states is another way to analyze the process of magnetization. Following Jaime *et al.* [42], we translate the spin Hamiltonian (Eq. 4.1) to an effective Hamiltonian of the hard-core boson:

$$\begin{aligned}\mathcal{H}_{\text{eff}} &= t_1 \sum_{\mathbf{i},\alpha} (b^\dagger_{\mathbf{i}+\hat{e}_n} b_{\mathbf{i}} + b^\dagger_{\mathbf{i}} b_{\mathbf{i}+\hat{e}_n}) + t_2 \sum_{\mathbf{i}} (b^\dagger_{\mathbf{i}+\hat{z}} b_{\mathbf{i}} + b^\dagger_{\mathbf{i}} b_{\mathbf{i}+\hat{z}}) \\ &+ V_1 \sum_{\mathbf{i},\alpha} n_{\mathbf{i}} n_{\mathbf{i}+\hat{e}_n} + V_2 \sum_{\mathbf{i}} n_{\mathbf{i}} n_{\mathbf{i}+\hat{z}} + \mu \sum_{\mathbf{i}} n_{\mathbf{i}} \end{aligned} \tag{4.2}$$

where the chemical potential is $\mu = J - g_{\parallel}\mu_B H$, and hopping terms are $t_1 = V_1 = J_1/2$ and $t_2 = V_2 = J_2/4$. The simulation shares the same interaction parameters with the spin model. Based on this reduced model, we calculate the magnetization and show the results with the red dashed curve in Fig. 4.6. In contrast to the result of $\mathcal{H}_{\text{spin}}$, the magnetization derived from $\mathcal{H}_{\text{eff}}$ shows the central symmetry that relates the magnetizations around H_{c1} and H_{c2}, which corresponds to the particle-hole symmetry shown in the middle insert of Fig. 4.6. However, in the following, we will see that such a symmetry is not held when the J_2-inter-dimer interactions in Eq. (4.1) is significant.

As shown in Fig. 4.6, the magnetization gradually increases with magnetic fields when the field approaches to and exceeds H_{c1}, while the magnetization drastically changes its slope at near the saturation field H_{c2} in our experiment. This behavior can be more clearly recognized in the $\mathrm{d}M/\mathrm{d}H$ curve; one can see that rather sharp peak structure appears just below H_{c2} and only a round shoulder structure is seen in the vicinity of H_{c1}. This asymmetric character of the magnetization indicates a sizable breaking of the particle-hole symmetry.

In order to clarify the asymmetric character, we utilize the following formula to perform the fitting of the magnetization.

$$|M - M_{ci}| \propto |H - H_{ci}|^{\beta_i}, \quad (i = 1, 2). \tag{4.3}$$

The breaking of the particle-hole symmetry can be identified by comparing

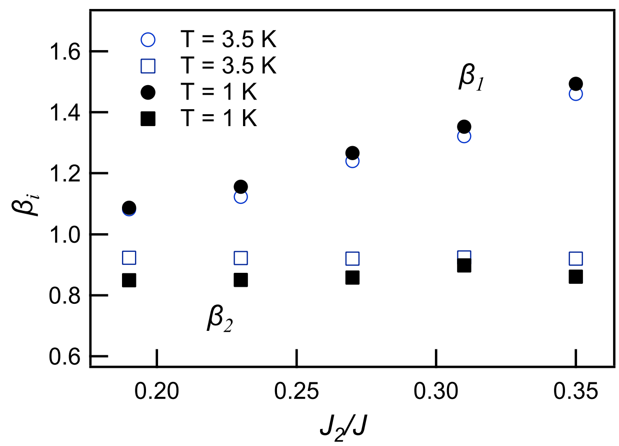

Figure 4.7: β_i (i = 1, 2) as a function of J_2/J with fixed $J_1/J = 0.201$. The determination is performed with simulated M-H at 3.5 K and 1 K. Circles and squares present β_1 and β_2, respectively. [50]

two critical exponents $\beta_{1,2}$ [1] around $H_{c1,2}$ in Eq. (4.3) since the particle-hole symmetry implies $\beta_1 = \beta_2$.

By analyzing our experimental data with the QMC simulation, we can computationally determine the critical exponents with the simulated M-H curve [54]. We find that β_2 is robustly localized at 0.91. Here $\beta_1 \sim 1.4$ is also obtained in the same analysis but using the experimental results obtained with a non-destructive magnetic field [15]. The amount of the difference between β_1 and β_2 directly measures the degree of the asymmetry, and the difference has been found to depend on the degree of the inter-dimer coupling (itinerancy of the triplons). We have conducted an analysis of the dependence of the exponents $\beta_{1,2}$ on the inter-dimer exchange interaction J_2. In the procedure for determination of $\beta_{1,2}$, we define field windows $x_{1,2} = (H - H_{c1,2})/(H_{c2} - H_{c1})$ which the data used should be within [11]. Accuracy of fitting process can be confirmed by stability of the obtained value when we change the field window. The fittings are performed under $x_{1,2} = 0.1$, 0.15 and 0.2. All the obtained exponents are plotted as a function of J_2/J in Fig. 4.7. The range of J_2/J is set from 0.18 to 0.35. As shown in Fig. 4.7, β_1 gradually increases with J_2/J while the value of β_2 is more

[1] Here, the critical exponents $\beta_{1,2}$ mean the the high-order term of variation, and considered to be "effective" critical exponent

robust. The resulted J_2-variations of β_1 and β_2 show similar behavior at 3.5 K and 1 K, indicating that the qualitative dependence of the critical exponents on the effects of the inter-dimer interaction is not affected by changing temperature from 1 to 3.5 K.

The differences between β_1 and β_2 are reflected by the convex slope of the magnetization around H_{c1} and H_{c2} as in Fig. 4.6; the initial magnetization process is suppressed compared to a linear magnetization while the slope increases when approaching the saturation, resulting in the larger β_1 than β_2.

In the bond operator theoretical formalism, the magnetism around H_{c1} is contributed by the outset of lowest-triplet $|\uparrow\uparrow\rangle$, namely $S_z = 1$-condensations driven by the vanishing spin gap. In the pure-dimer limit $J \gg J_{1,2}$, the other two higher-energy local excitations ($|\uparrow\downarrow\rangle + |\downarrow\uparrow\rangle$) and $|\downarrow\downarrow\rangle$ can be neglected since they hardly affect the low-temperature physics. However, a finite J_2 interaction can mediate a four-particle interaction that accumulates highest-triplet $|\downarrow\downarrow\rangle$ excitations in the presence of a partial lowest-triplet condensation and singlet condensation [45]. Therefore, $|\downarrow\downarrow\rangle$ excitations suppress the magnetization from the $|\uparrow\uparrow\rangle$ condensations when $H \gtrsim H_{c1}$. When the magnetic field increases beyond H_{c1}, such a suppression eventually becomes inefficient due to a large Zeeman gap to excite a $|\downarrow\downarrow\rangle$ quasiparticle and is neglibible near H_{c2}. Therefore, we have the increasing deviation of β_1 from β_2 as shown in Fig. 4.7. The convex shape of the M–H curve at around H_{c1} can be understood in the same way. Moreover, it is found that β_2 is consistently insensitive to a changing of J_2/J. In short, the deviation of β_1 from β_2 is attributed to the strength of J_2-inter-dimer interactions. Therefore, it can be concluded that the particle-hole symmetry in the hard-core boson picture (Eq. 4.2) is broken in $TlCuCl_3$ due to the strong higher-order terms through the inter-dimer interactions. Here, it should be noted that the similar inter-dimer effect is also obtained by increasing J_1 instead of J_2. The hybridization of the four-particle states becomes relevant when J_1 or J_2 (or both) is (are) sufficiently large.

Such a particle-hole symmetry breaking has been observed in another spin-1/2 dimer system [55]. In that case, the origin of the asymmetry is claimed to be due to a zero-point quantum fluctuation characterized by the additional zero-point energy to quasi-particle excitations [56], which should be signifiant in low dimensional systems. However, such a quantum fluctuation in low dimensions is expected to be insignificant in $TlCuCl_3$ because the spin system is almost three-dimensional [2].

Furthermore, due to the insignificance of higher-energy triplet excitations around the saturation, it can be expected that the H-T phase boundary around H_{c2} obeys a power law $g|H_s - H_{c2}(T)| \propto T^\alpha$ (H_s: the saturation field strength at zero temperature) closer to the HFP approximation $\alpha = 1.5$ [3] than that regarding Eq. (2.1) around H_{c1}. It implies that the strong inter-dimer interactions contribute to a remarkable dispersion in the dimer spin system. This dispersion can be understood by magnon-magnon or hole-hole interaction in a boson system. Thus we have proved that the dispersion of the particle manifests itself in the asymmetric convex magnetization process, which indicates that a precise measurement of the magnetization can give us microscopic nature of magnons in some particular magnets.

In summary, we have measured the magnetization process of $TlCuCl_3$ at 2 K and the second critical magnetic field H_{c2} to be 86.1 T. The magnetization process shows a continuous convex slope and we analyze the critical exponents of magnetization at H_{c1} and H_{c2}. A Monte Carlo calculation based on cubic lattice well reproduces the experimental results and strongly supports the itinerant property of magnons in $TlCuCl_3$. The particle-hole symmetry has been revealed to be broken in $TlCuCl_3$. We have also found that the degree of asymmetry of magnetization process increases with the inter-dimer interactions by a numerical analysis with the QMC method. Thus, such interactions play an essential role in magnetization of various spin dimer systems.

[2]Because the rate of magnetic susceptibility between H_{c1} (5.6 T) and H_{c2} (86.1 T), i.e. χ_1/χ_2 in $TlCuCl_3$ is as large as 5 (see Fig. 1) which is 2.5 times larger than that of $NiCl_2$-$4C(NH_2)_2$ Ref. [56], the renormalized mass m* is expected to be reduced by a factor of $(2.5)^{3/2}$ ~4 compared to the case of Ref. [56]. Therefore the m/m* in $TlCuCl_3$ should be as large as $3 \times 4 \sim 12$. This seems to be too large for 3-dimensional spin system $TlCuCl_3$, and thus the quantum fluctuation may not be the origin of the asymmetry in $TlCuCl_3$.

Chapter 5

Spin liquid state and α-$RuCl_3$

5.1 Heisenberg-kitaev model and possible realization in α-$RuCl_3$

This section mainly introduces the physical properties of ruthenium trichloride and related theoretical predictions.

The crystal structure is shown in figure 5.1 [27]. The space group is C/2m. The edge sharing octahedral layer of $RuCl_6$ is vertically stacked to form the honeycomb layer with an offset in the plane. The ground state of ruthenium trichloride is antiferromagnetic. As we mentioned above, according to the prediction of the Heisenberg-Kitaev and other models, the possible ground states in the honeycomb lattice include zigzag, stripy and so on, with the changing of exchange interaction parameters. The arrangement of these ground states is given in figure 2.7 [27]. Elastic neutron diffraction can help to determine the antiferromagnetic arrangement in the ground state. The neutron results of Johnson et al. (figure 5.2) indicate that a zigzag Bragg peak is significant in α-$RuCl_3$, indicating that its ground state is zigzag arrangement. A natural question is whether the spin liquid state emerge after the Zigzag state is broken or suppressed.

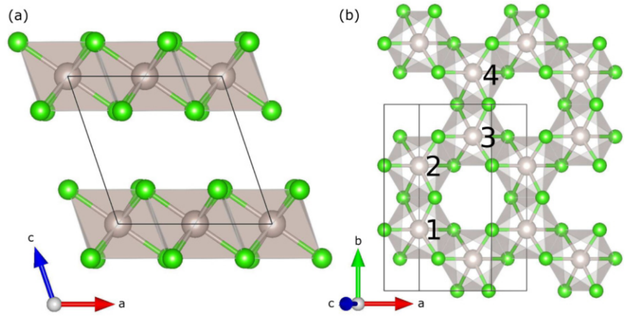

Figure 5.1: Crystal structure of α-$RuCl_3$ [27].

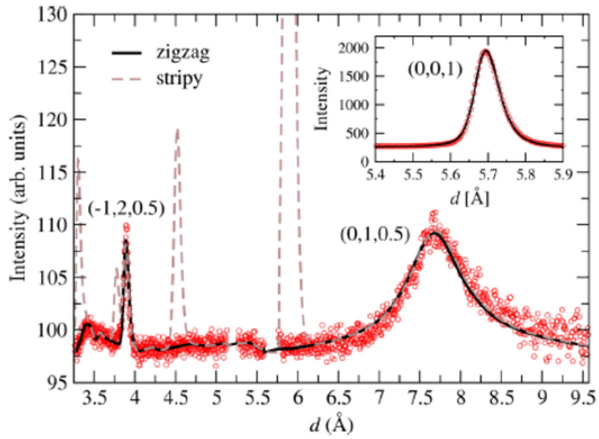

Figure 5.2: Elastic neutron diffraction for α-$RuCl_3$ [27].

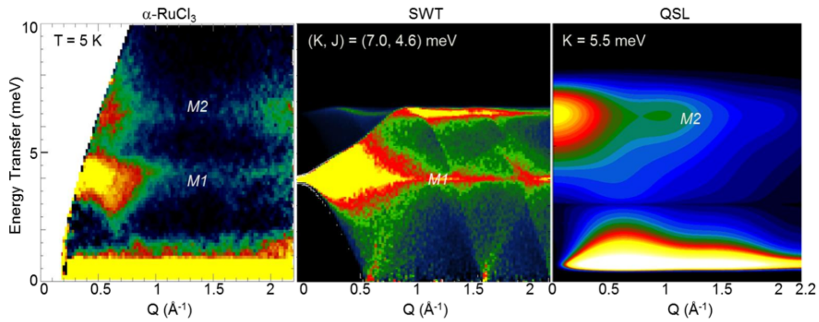

Figure 5.3: Inelastic neutron diffraction for α-$RuCl_3$ at 5 K and zero-field [57].

Early inelastic neutron diffraction focused on whether Kitaev interaction could be achieved in α-$RuCl_3$. Banerjee et al. [57] first reported the results of inelastic neutron diffraction at 5 K, as shown in Figure 5.3 (left). In this result, two clear modes, M1 and M2, are observed in the vicinity of 4 and 6 meV. By comparing the theoretical calculation results of spin wave and pure Kitaev calculation results (Figure 5.3 (mid) and (right)), Banerjee et al. argued that the excitation energy spectrum of zigzag order obtained by the spin wave theory was inconsistent with that of M2 mode. Pure Kitaev spectra, however, consistent with the M2 mode well. Therefore, they believe that Kitaev interaction is present in α-$RuCl_3$.

Do et al. [58] first reported the effect of temperature on the ordered phase destruction of α-$RuCl_3$. In their experiments, the temperature dependence of magnetic susceptibility, specific heat and entropy were measured respectively. The results are shown in figure 5.4. In these macroscopic measurements, all order parameters show two significant changes. Do et al. defined the two changing temperature points as T_N and T_H. They claim that between T_N and T_H, the system is in a region of Kitaev paramagnetic state. Both the local and the itinerant Majorana fermion exist in this region. When the temperature become higher than T_H, these Majorana fermion excitations are destroyed and the system becomes a traditional paramagnetic state (as shown in figure 5.5). This assumption was also confirmed by their inelastic neutron scattering experiment, in which the inelastic neutron scattering observed a continuous excitation spectrum at the γ point between T_H and T_N. This continuous excitation gradually disappears when the temperature exceeds T_H.

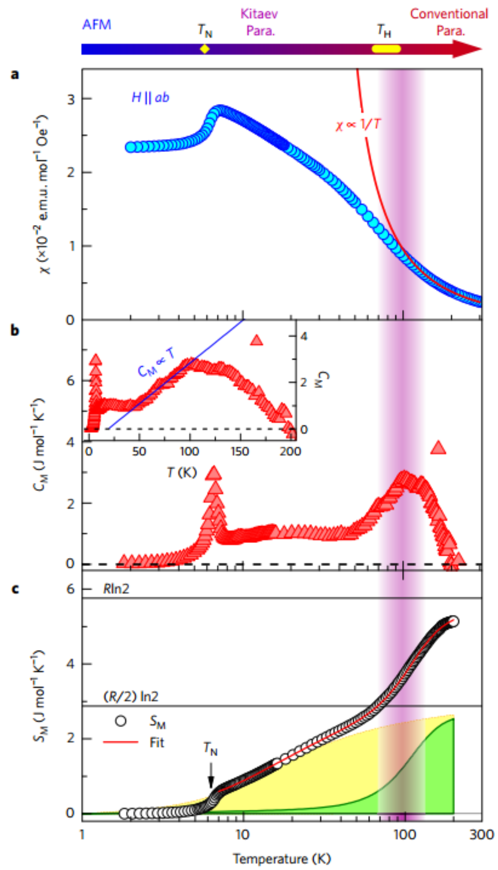

Figure 5.4: Temperature dependence of magnetic susceptibility, specific heat and entropy for α-RuCl$_3$ [58].

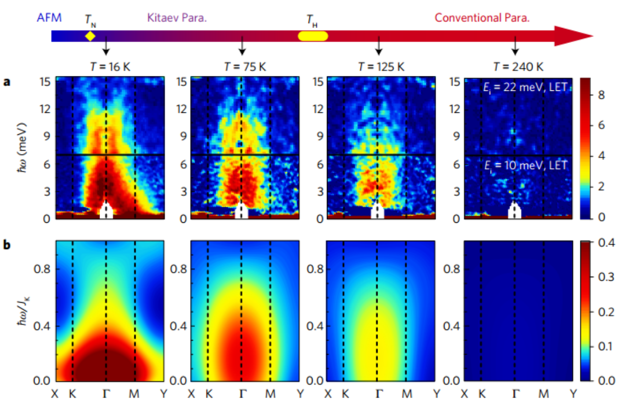

Figure 5.5: Inelastic neutron diffraction for α-RuCl$_3$ at different temperature [58].

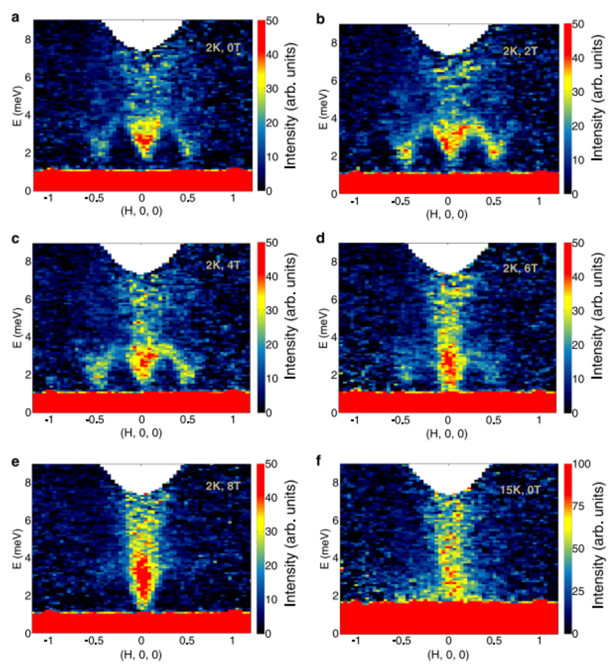

Figure 5.6: Inelastic neutron diffraction for α-RuCl$_3$ under external field [59].

The results of another study by Banerjee et al. [59] are highly similar to those of Do et al. They also observed the properties of the 15 K continuous excitation, as shown in figure 5.6 f. On this basis, the influence of external magnetic field along ab direction is also studied. As shown in Figure 5.6 a-e, at the temperature of 2 K, when the external field is less than 6 T, the diffraction pattern shows a clear magnon signal. The signal gradually disappears with the suppression of magnetic field. Under the external magnetic field between 6 and 8 T, the continuum excitation at the gamma point becomes clearer. The continuum excitation is similar to the one at 15K, indicating that the suppression by magnetic field and the destruction of ordered phase by temperature have similar effects. This also suggests that the system might resemble a spin liquid state under the suppression of magnetic field. Meanwhile, Banerjee et al. also measured susceptibility, as shown in Figure 5.7, with two very distinct peaks of susceptibility at 6.1 and 7.3 T. Banerjee et al. claimed that the peak around 6.1 T may imply an entering into an intermediate phase between the field-induced spin liquid and the ordering phase.

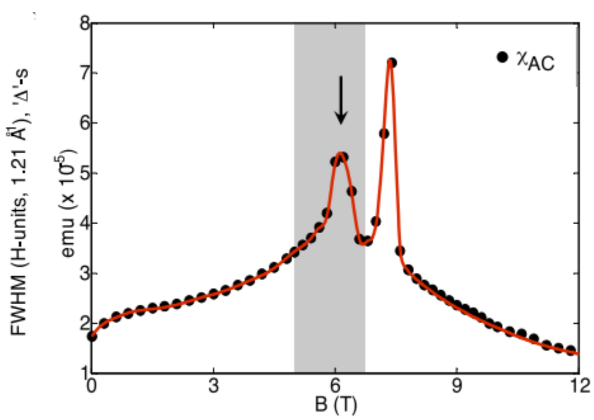

Figure 5.7: Magnetic susceptibility for α-$RuCl_3$ under external field along ab plane [59].

Wellm et al. [60] reported similar results on their ESR experiment, as shown in figure 5.8. They studied the absorption spectrum of α-$RuCl_3$ under the external field along ab plane using electromagnetic waves of 70-660 GHz. The results showed that the absorption peaks of α-$RuCl_3$ show frequency independence in the range of about 6-8 T. This means that α-$RuCl_3$ exhibits a continuum excitation under an external field about 6-8 T, which is consistent with the properties of quantum spin liquids.

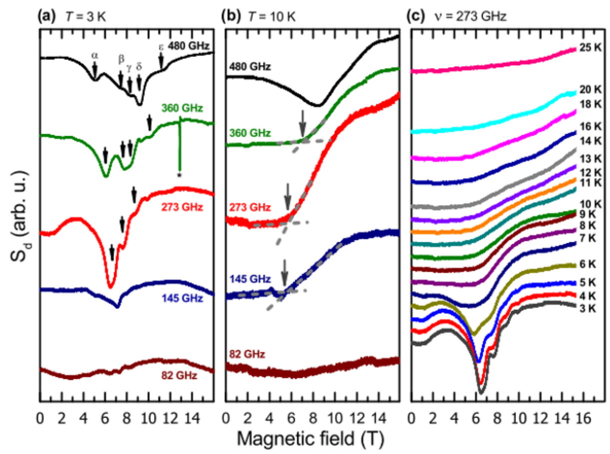

Figure 5.8: ESR measurement at intermedia field region [60].

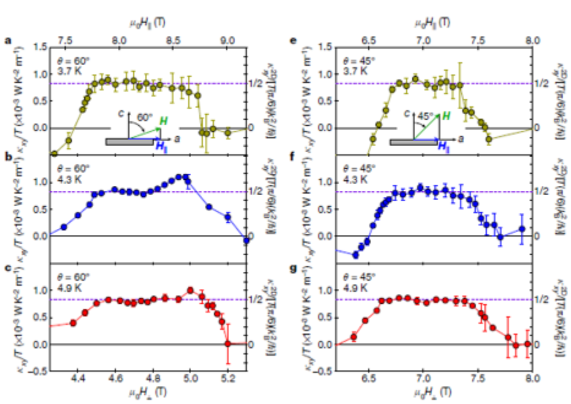

(a)

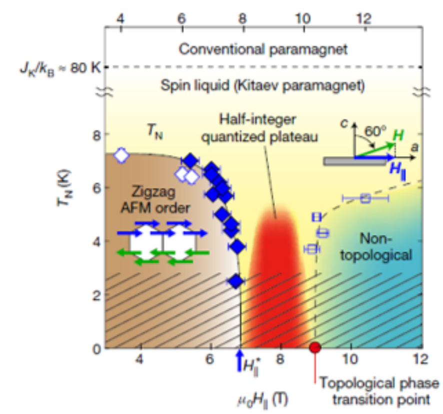

(b)

Figure 5.9: Thermal quantum Hall effect of α-RuCl$_3$ under external field along different angles [61].

More recently, the results about thermal quantum Hall effect reported by Kasahara et al [61] have been more encouraging. As shown in Figure

5.9, they observed a half-integer thermal Hall conductivity at the similar magnetic field region. In addition, the field-region of thermal Hall effect changed with the rotation of the angle between the magnetic field and the ab plane. With the increase of the angle between the external field and ab plane, the range of the thermal Hall effect gradually moves to the higher field region, as shown in Figure 5.9.

For the condition that the external field perpendicular with ab-plane, only few studies are reported because the measurement techniques under high magnetic field environment are still rigorous. Kuboda et al. [28] reported their magnetization up to 60 T along c* axis as early as 2015, as shown in figure 5.10 (a). The c* is defined as the direction perpendicular with the honeycomb ab-plane. A similar measurement is also reported by Johnson et. al. [27] as shown in figure 5.10 (b). What their results in common is that magnetization is far from saturated even up to 60 T, although the observed magnetization process of them is totally different in the case of field along c* axis.

Modic et al. [62] recently reported the angle-rotation dependence of torque for α-$RuCl_3$, as shown in Figure 5.11 (a). The angle-rotation dependence of critical field shows a bowl-like shape. The tendence of this bowl-like shape is similar with the predicted results based on exact diagonalization calculation in Ref. [63], although the detail is somehow different, as shwon in figure 5.11 (b). This experimental result didn't show the intermediate phase under external fields.

Experimental and model studies of α-$RuCl_3$ have made great progress, but many problems remain to be solved, as shown below:

1) The full-spin Hamiltonian of α-$RuCl_3$ is still unclear. In general, neutron scattering can determine the Hamiltonian of a spin system; however, in α-$RuCl_3$, many different models satisfy the neutron experimental results. In Ref [64], a summary of proposed parameters are listed in Table 5.1. The susceptibility calculated by the ED method is given in figure 5.12 (2-9 listed in table 5.1 corresponds to a-h in figure 5.12). There are still contradictions between these results and experimental results [27, 60].

2) Nature of the field-induced topological phase with continuum excitation are still unclear. The key to solve this problem is also determining the full-spin Hamiltonian of α-$RuCl_3$.

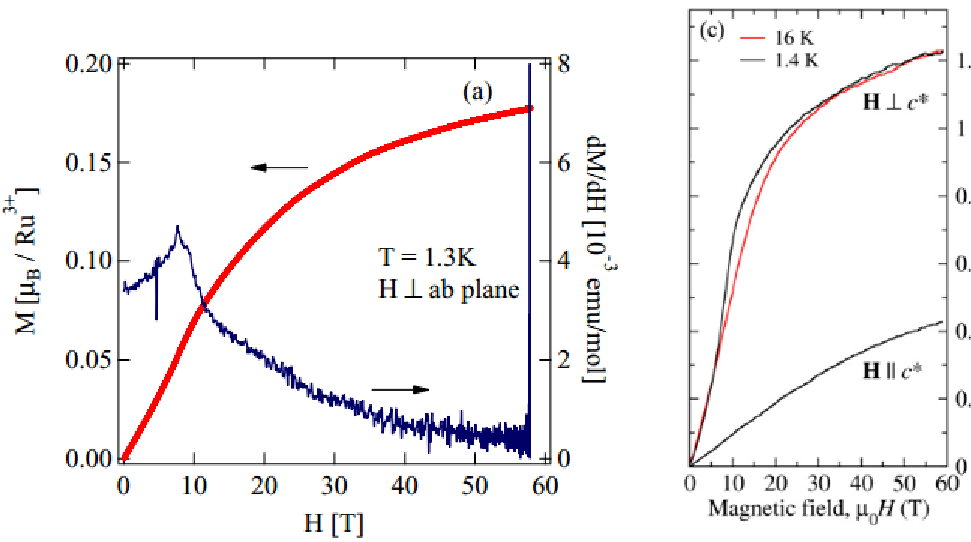

(a) (b)

Figure 5.10: The magnetization process up to 60 T, (a) from Ref. [28], (b) from [27]

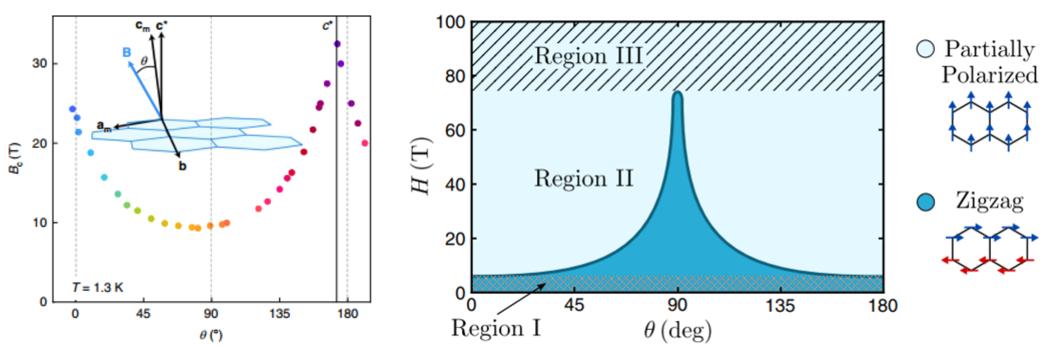

(a) (b)

Figure 5.11: a, angle-field phase diagram from torque experiment [62]; b, angle-field phase diagram from ED calculation [63].

3) The experimental results reported in different literatures are still contradictory. For example, no intermediate phase was observed in the torque experiment, the magnetization results in the direction of c* were also different [27, 28, 60, 62] and so on.

In this study, the magnetization of α-$RuCl_3$ at different angles of ab-plane-field was measured by using the destructive and non-destructive pulsed magnetic fields. The results show that α-$RuCl_3$ saturated at about 90 T with field perpendicular to ab-plane, which is similar to the prediction of about 80 T calculated by ED [63]. In the low magnetic field range, an intermediate phase is observed at different angles, which is similar to the report of Ref [28, 57, 61]. A rough angular-magnetic field phase diagram is given in this study. Our experimental results are still inconsistent with some previous report in Ref. [62], and the reasons are still unclear.

Set	K_1	Γ	J_1	J_2	J_3	K_3	Pattern	NIP	
								h_b	h_{c^*}
1	7		-4.6				Zigzag	0	1
2	-5	2.5	-0.5		0.5		Zigzag	0	0
3	-10.6	3.8	-1.8		1.25	0.65	Zigzag	0	0
4	-6.8	9.5					ID	0	0
5	-5.5	7.6					ID	0	0
6	-8	4	-1				ID	0	0
7	-6.6	6.6	-1.7		2.7		Zigzag	0	0
8	17	12	-12				120^0	1	0
9	-5.6	-1	1.2	0.3	0.3		120^0	1	0

Table 5.1: Summary of numerical results for finite magnetic fields for various sets of parameters [64].

5.2 Magnetization process of α-$RuCl_3$ up to 100 T

5.2.1 experiment detail

A single crystal of α-$RuCl_3$ was used for the experiments. The α-$RuCl_3$ sample in this experiment was provided by Prof. Tanaka of Tokyo Institute

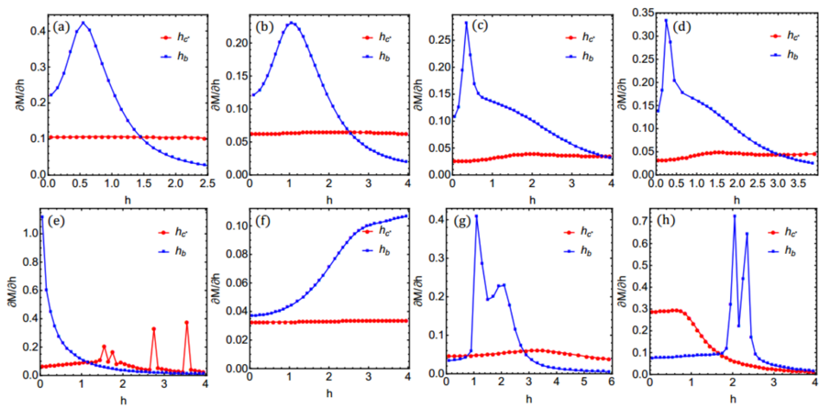

Figure 5.12: dM/dh curves calculated by ED calculation based on the parameters list in table 5.1 [64]

of Technology. The sample is shown in figure 5.13 (a). It should be noted that the samples of α-$RuCl_3$ are very soft and an unintentionally applying pressure has a great influence on their physical properties. Therefore, the problem regarding fixation and the pressure of α-$RuCl_3$ should be treated carefully during the measurement. In this experiment, vacuum silicone grease and glass rods were used to fix the α-$RuCl_3$ sample. As shown in Figure 5.13 (b), two glass rods with a fixed-angle incline sandwiched the α-$RuCl_3$ sample. The surface of α-$RuCl_3$ is coated with a thin layer of vacuum silicone grease. At low temperature, the vacuum grease gradually hardens, thus, fixed α-$RuCl_3$. The magnetization curves of the samples were measured at different ab-plane-field angles separately, as shown in figure 5.13 (c). The magnetization process of 0, 60, and 70 degrees were measured under the non-destructive magnetic field in collaboration with Kindo group. The measurement techniques are introduced in Sec. 3.2.2. The measurement for external field perpendicular with the ab plane is performed under the destructive magnetic field. The realization of low temperature environment is same with the $TlCuCl_3$ in Chapter 4.

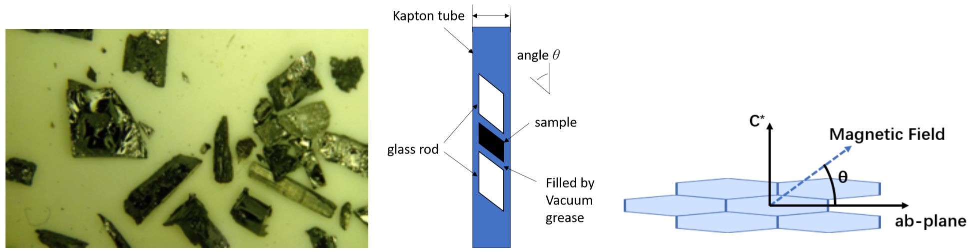

(a) (b) (c)

Figure 5.13: a: Single crystal of α-$RuCl_3$. b: Sketching of fixed α-$RuCl_3$ by glass rod. c: Sketching of rotation of magnetic field.

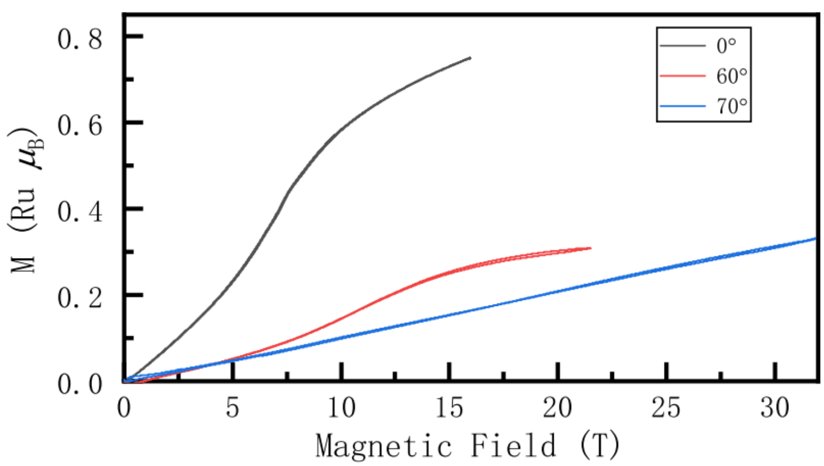

Figure 5.14: Magnetization process at different θ up to 30 T.

5.2.2 Result and discussion

Figure 5.14 shows the measurement results of the magnetization process under non-destructive pulsed magnetic field. The angle θ between the ab plane of sample and the magnetic field are given in this experiment, as shown in Figure 5.13 (c). Magnetization processes at different angles are shown in figure 5.14. Within the range of experimental sensitivity, the M-H curves for ascending and descending parts of the field pulse are indistinguishable

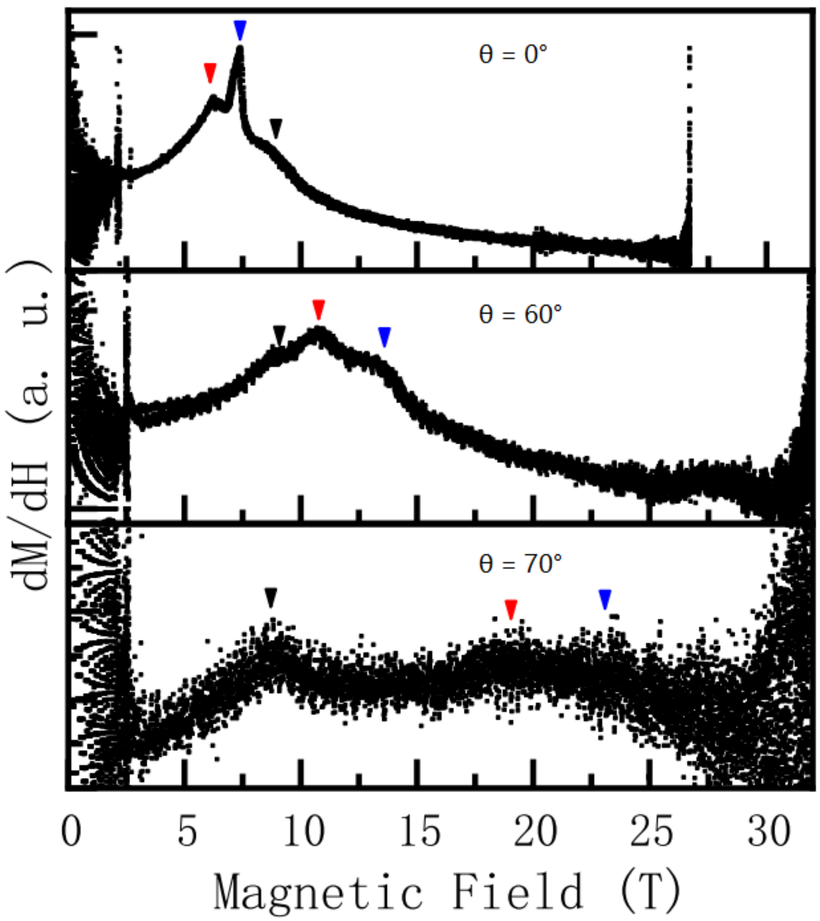

Figure 5.15: Field dependence of susceptibility under different θ (red: H_{c1}, blue: H_{c2}, H_{imp}).

(i.e., with little or no lag). The magnetization of the sample approaches saturation rapidly for $\theta = 0$, which is consistent with previous reports. With the increasing angle θ, the slope of magnetization process gradually slows down, and the sample exhibited a strong anisotropy. This anisotropy has been pointed out to be due to the Heisenberg interaction or Γ-term interaction effects. Figure 5.15 shows the field-dependent susceptibility at different angles. Three clear signals are labeled with the triangle mark. The magnetic susceptibility observed at 70 degrees is very noisy probably due to the effect of magnetic anisotropy. However, the signals are still observable clearly. The three peak position here are marked by red, blue, and black triangle and are defined as H_{c1}, H_{c2}, and H_{imp}, respectively. As increasing θ, H_{c1} and H_{c2} gradually shift towards the high field region, while H_{imp} remains basically unchanged. Although the H_{imp} signals are also reported in Ref. [28], it is not reported in Ref. [59]. Since H_{imp} is independent of θ, we consider it as an impurity signal here. It also maybe caused by a disorder owing to an accidental AB stacking [62]. Here we define the phase between H_{c1} and H_{c2} as a intermediate phase.

Figure 5.16 shows the magnetization process and dM/dH curve at 2 K, under an eternal field perpendicular to the ab plane, i.e., $\theta = 90°$. The gray open dot is the raw dM/dH data. Because the single-turn coil is employed, the dM/dH data below 60 T are very noisy. The black curve is the smoothed dM/dH curve. The magnetization process is obtained by integrating dM/dH data, which is the same as the process of Sec. 4.2. Because the raw dM/dH data is too noisy, we only analyze the smoothed dM/dH curves. At about 25 T and 35 T, the smoothed dM/dH curve shows two very weak peaks. Although the possibility that the two peaks are from noise cannot be ruled out, the hill-like hump of dM/dH curve from 20 T to 40 T hints these two peaks are signals. At about 80 T, the dM/dH curve presents a broad peak, indicating a magnetic phase transition into saturation.

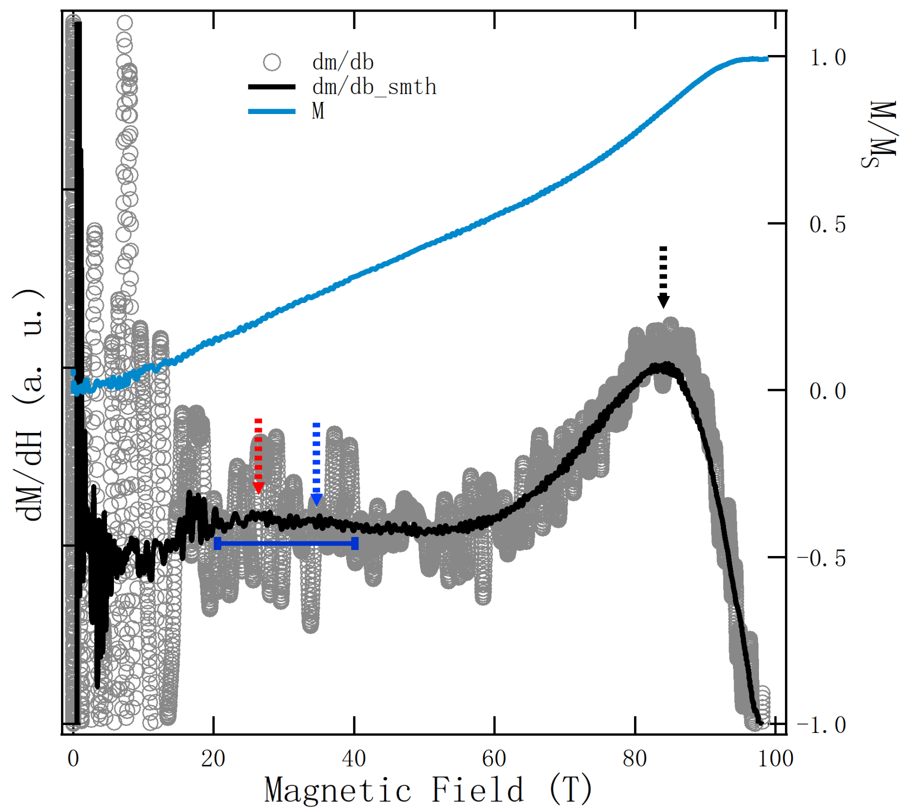

Figure 5.16: M-H and dM/dH curves measured by single-trun coil.

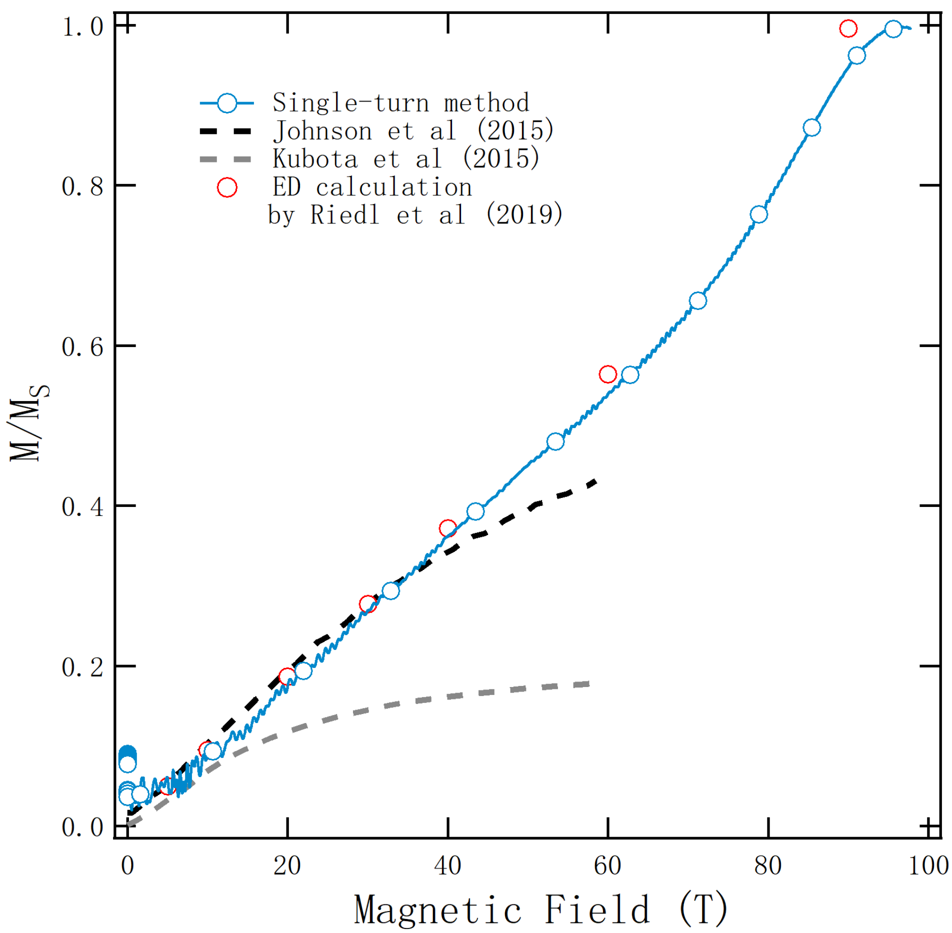

Figure 5.17: Comparison between the data of this work and previous report. The dash line data are from Ref. [27, 28], and the ED calculation results are from Ref. [63].

In Figure 5.17, we compare the results from Ref. [27, 28] with our measurement results. The blue gray and the blue dash curve are the results reported by Johnson and Kubota, respectively. The measured magnetization process is similar to the results of Johnson et al. below 40 T, but show difference above 40 T. On the other hand, Kubota's results are totally different from our magnetization process. The reasons for the difference are still unclear. It may be from the deformation of samples under an ultrahigh magnetic field. The ED calculation by Riedl et al. [63] is also shown in Figure 5.16 by blue open circles. Although the ED results are not consistent with our results exactly, it is interesting that they show good agreement if multiplying by a factor of 1.05, which indicated that the parameters in Ref [63] are close to the full-spin hamitonain of α-RuCl$_3$.

H (T) \ θ	0°	60°	70°	90°
H_{c1}	6.1	10.8	18.9	25
H_{c2}	7.3	13.2	23.6	34
H_s	-	-	-	83

Table 5.2: Summary of numerical results for finite magnetic fields for various sets of parameters

The two weak peaks in Figure 5.16 are defined as H_{c1} and H_{c2} following the definition in Figure 5.14, respectively. The critical field before saturation (broad high peak) is defined as H_s. Table 5.2 shows the values of all critical magnetic fields at different angles. Meanwhile, the phase diagram of θ-field is given in Figure. 5.18. This result is consistent with previous reports by Ref [28, 57] for the case $\theta = 0$. H_{c1} and H_{c2} measured at different angles form an intermediate region. This intermediate may be related to the field-induced spin liquid. A similar conclusion is also reported in Ref. [60]. As increasing angle θ, this intermediatete phase gradually moves towards the high-field region, which is same with the tendency reported in Ref. [61], which is a the thermal Hall effect measurement. It also implies that this intermediate phase has correlation with the spin liquid phase. In Ref. [62], it is reported that this multimagnetic phase transition may be caused by defects owing to an accidental AB stacking. However, some of the calculated results in Ref [64] (see in Fig. 5.12) support that the intermediate phase is an intrinsic result of some full-spin hamitonians, although the ground states calculated by these parameters are still not consistent with the current experimental results.

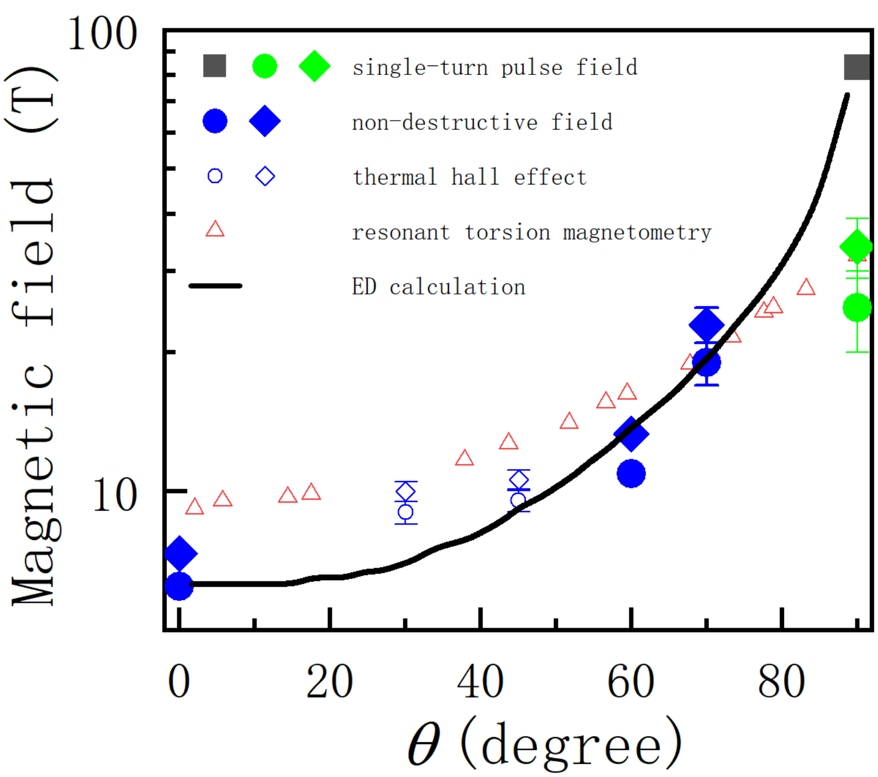

Figure 5.18: Phase diagram based the current data. Results of this work are represent as big mark, open red triangle are from Ref. [62], open blue circle are from Ref. [61], black curves are ED calculation results from Ref. [63]

In order to clearly compare our results with those of the previous reported data, I make a rough phase diagram based on existing data as shown in figure 5.18. The experimental results obtained in this study are represented by solid markers, and the critical fields obtained from smoothed data are represented by the green solid marks. Other open markers represent the results of the previous studies. The calculated results based on torque experiments are shown by black curves in the figure. Interestingly the tendencies of the phase boundary obtained by magnetic field angle dependence experiment are similar in different experimental results of studies. This also means that there are possible spin liquid phase in the intermediate phase near the phase boundary or above the phase boundary for the high θ region, where the neutron or ESR experiment are still limited because of a high magnetic field requirement. The determination of this possibility is expected by measuring a variety of order parameters at more angles θ.

5.3 Summary

In this study, we measured the magnetization process of α-$RuCl_3$ under different magnetic field angles. A whole magnetization process under a field perpendicular to ab plane ($\theta = 90°$) has been reported for the first time. Based on the measured results, we find that there is a θ-dependent intermediate phase. This intermediate phase is likely to be a spin liquid phase, or strongly associated with a spin liquid phase. Our observations of the magnetization process contributes to the hunting of the full-spin Hamiltonian of α-$RuCl_3$.

Chapter 6

Magnetoresistance of YbB_{12} up to 120 T

6.1 Physical property of YbB_{12}

The Kondo insulator YbB_{12} was discovered by Kasaya et al in 1983. Figure 6.1 shows the crystal structure of YbB_{12} [65]. The structure is a NaCl face-centered cubic lattice. Yb occupies the Na lattice and B_{12} cluster occupies the Cl lattice. The B_{12} cluster is octahedron, and the valence electrons are $2s^2$ and $2p^1$.

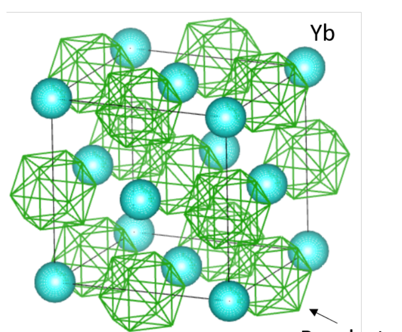

Figure 6.1: Crystal structure of YbB_{12}

Figure 6.2 shows the temperature dependence of resistance and Hall resistance [66]. At high temperatures, the resistance is metal-like, while at low temperature it is semiconductor-like. Figure. 6.3 shows the temperature dependence of magnetic susceptibility [66]. From a room temperature to about 100 K, the magnetic susceptibility increases with decreasing temperature. But below 100 K, the susceptibility decreases dramatically. Magnetic susceptibility increases near the lowest temperature. Based on a NMR measurement it is found that the increase is due to the influence of impurities. The ground state is paramagnetism at low temperatures. Thus, at high temperatures it is a normal paramagnetic metal, and at low temperatures it is an insulator (semiconductor) with charged and spin gap.

One interesting point of YbB_{12} is the fluctuation of valence. Figure 6.4 shows the temperature dependence of the valence number [67]. The valence number of Yb increases with temperature. However, even in 200 K, Yb ions do not become Yb^{3+}, which implies that strong fluctuation and hybridization of valence electron are related to the formation of energy gap.

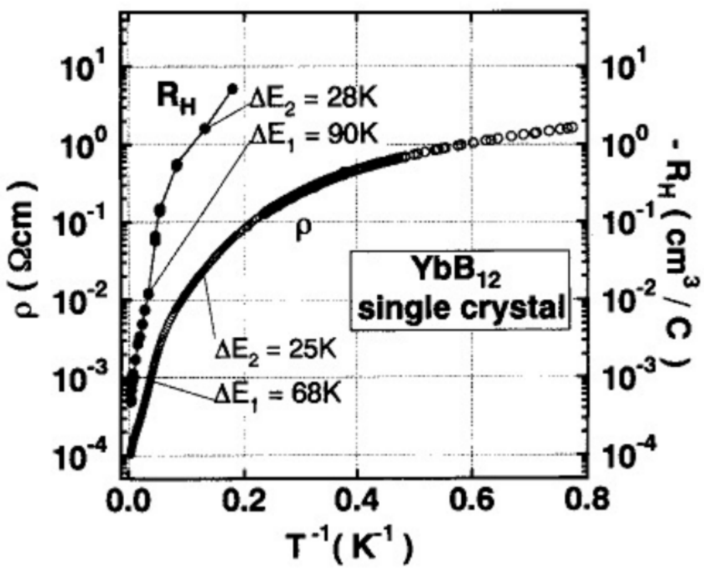

Figure 6.2: Temperature dependence of resistance and Hall resistance [66].

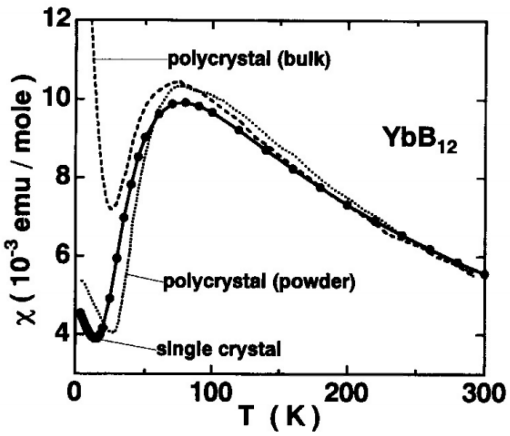

Figure 6.3: Temperature dependence of susceptibility [66].

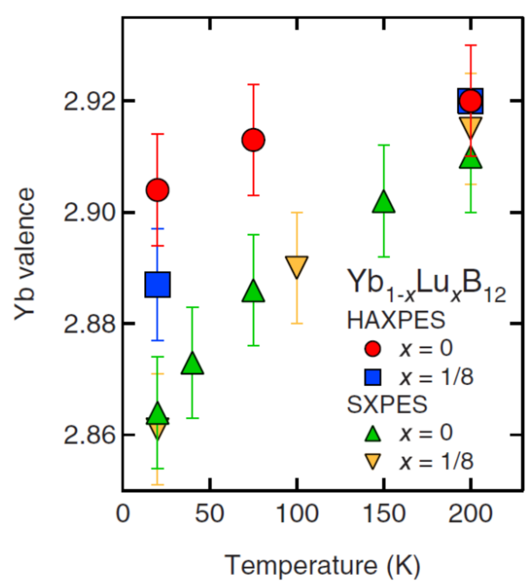

Figure 6.4: Temperature dependence of the valence number [67].

In general, the magnetic moment saves energy when a magnetic field is applied, and to a system tends to be integer valence state. For Yb, it is going toward the direction of Yb^{3+} (J = 7/2). The valence is sensitive to the magnetic field when the hybridization is weak, and the phase transition is easily observed in low magnetic fields. However, if the hybridization is strong, a strong magnetic field is necessary.

Figure 6.5 shows the magnetic field dependence of X-ray absorption of YbB_{12} [68]. The expected change in X-ray absorption should be measured when the component of Yb^{2+} is converted to Yb^{3+} in the magnetic field. At least until 50 T there's no change or little change in valence.

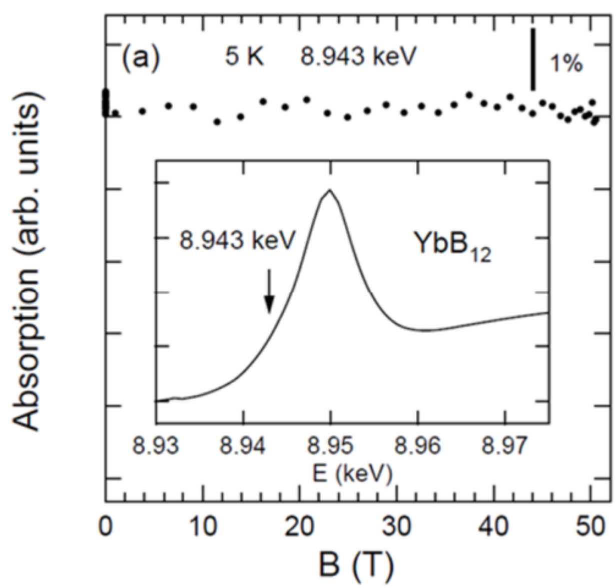

Figure 6.5: The magnetic field dependence of X-ray absorption [68].

The Kondo insulator YbB_{12} has a charge gap of 15 meV. According to the determination of DOS by photo emission spectrum [69], as shown in Figure 6.6, the spectrum shows a 15 mev peak structure at low temperature. The peak intensity of 15 mev increases from about 110 K, while the Fermi energy intensity decreases from that temperature. In addition, there are peak signals at 15, 25, 30 and 45 meV as well. It is generally, 30 meV and 45 meV peaks are considered to be related to crystal field and 4f electron (J =7/2), respectively. Interestingly, the peak of 25 meV becomes stronger below 200 K, which is similar to the 240 K of kondo temperature of YbB_{12}. Therefore, it is speculated that this is the energy gap caused by the Kondo effect, and YbB_{12} is thought to have two energy gaps in the zero magnetic field [69].

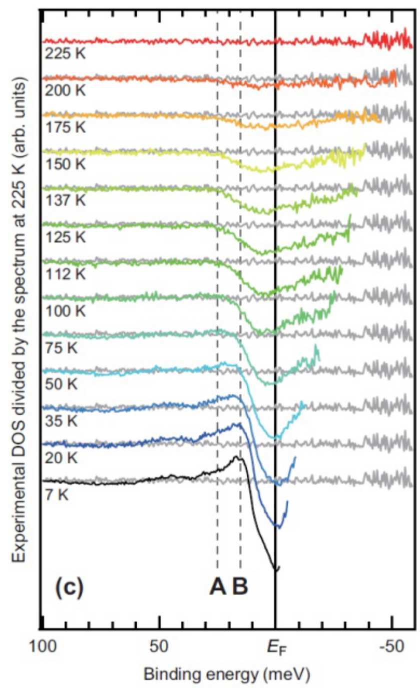

Figure 6.6: DOS by photo emission spectrum [69].

Magnetic field induces YbB_{12} to undergo insulator-metal phase transition. Figure 6.7 (a) and (b) show the results of magnetization measurement and electric resistance measurement [70]. The major feature is the emergence of magnetism and insulator metal transfer at around 50 T (Figure. 6.7 b). In addition, when a magnetic field is applied in the direction of [001] [110] [111], the critical magnetic field and the magnetization value at 68 T is also different. The critical field for field parallel to b-plane is smaller than the other directions, and the magnetization value at 68 T is also the smallest. Until 68 T, no saturation of magnetization has been observed in any direction. In addition, the resistance keeps a constants after YbB_{12} becomes a metal.

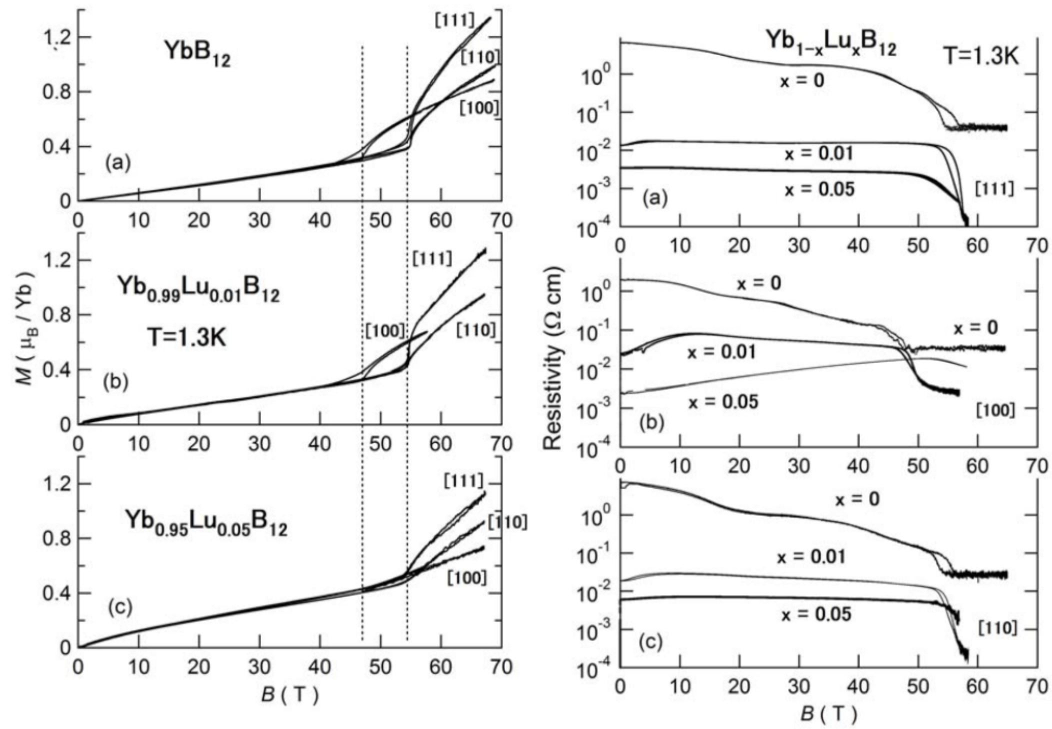

(a) (b)

Figure 6.7: (a) Single crystal of α-$RuCl_3$. (b) Magnetoresistance of YbB_{12} up to 70 T. [70]

FIG. 6.8 shows temperature- and field- dependence of resistance[1]. The phase transition can be clearly seen at low temperature, but the magnetic field dependence is hardly seen at high temperature. In addition, the resistance values after the phase transition are also different at different temperatures.

[1]K. Takeda master thesis

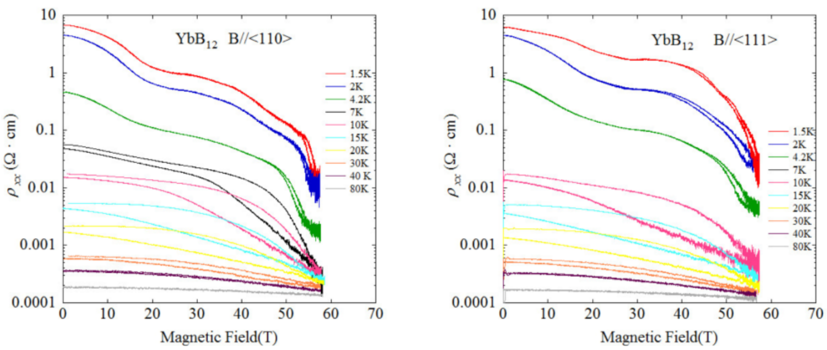

Figure 6.8: The temperature- and field- dependence of resistance[2].

The simplest model to describe the insulator-metal phase transition in Kondo insulators is the spin singlet state formed by the conduction-electron and f-electron. The increasing temperature can break the spin singlet state, which thus breaks the energy gap, leading to the insulator-metal phase transition. The magnetic field closes the energy gap in the same way. When the magnetic field destroys the spin singlet state, the system becomes a metal.

In a previous study of ultra-high magnetic field, Terashima [71] measured the magnetization process up to 120 T, as shown in figure 6.9. The results of dM/dH show that there are two magnetic phase transitions at around 50 T and 100 T respectively, which means that there are two peaks in the DOS, as shown in figure 6.10. The crossover of spin up and spin down leads to the increase of magnetization. This means that a phase transition at 100 T may give a lower resistance of YbB_{12} than at 50 T. A natural question is whether this phase transition transforms YbB_{12} into a normal metal. Considering that the saturation magnetization of YbB_{12} should be 4, since the expected saturation magnetic moment of Yb^{3+} is 4 μB, YbB_{12} may have further phase transitions at higher magnetic fields. In order to check this idea, it is necessary to measure the resistance of YbB_{12} at around 100 T.

[2]K. Takeda master thesis

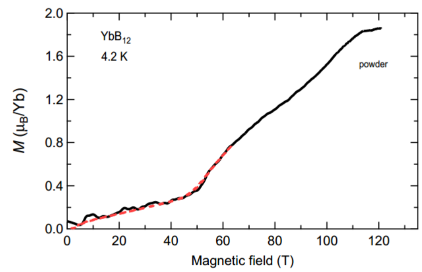

Figure 6.9: Magnetization process up to 120 T [71].

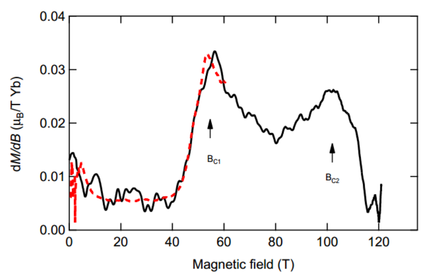

Figure 6.10: dM/dB for magnetization process up to 120 T [71].

Previous work has shown that YbB_{12} becomes metal around 50 T. So measuring the electric resistance of the bulk in a single-turn coil pulse magnetic field is not feasible because of the huge Joule heat problem. So far, there have been no reports on measuring resistance at 100 T magnitude in powder samples. In this study, we measured the resistance of YbB_{12} up to 120 T using the new method described in Chapter 3. The experiment was performed at 4.2 K.

6.2 Magnetoresistance of YbB_{12}

The method to measure the magnetoresistance of powder has been introduce in Sec. 3.3. Here, I only introduce some details of the pickup coils. Two types of coil are employed in this experiment. The schematic graph of two types coils are shown in figure 6.11 (a) and (b), named as I- and II-type coil.

The difference of two types coils is the configuration of input coil and output coil, where I-type is a covered relationship and II-type is string-like shape.

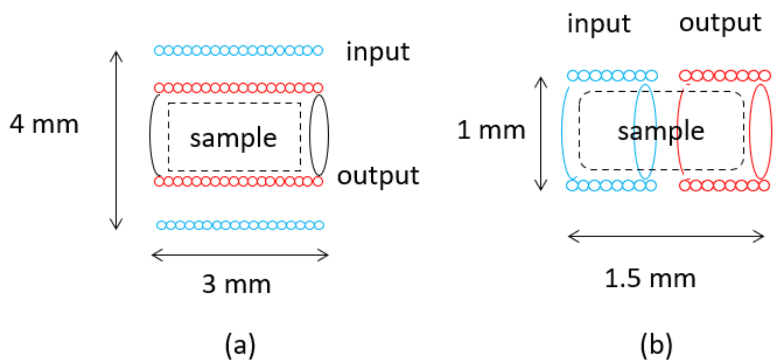

Figure 6.11: Schematic graph of two type coils.

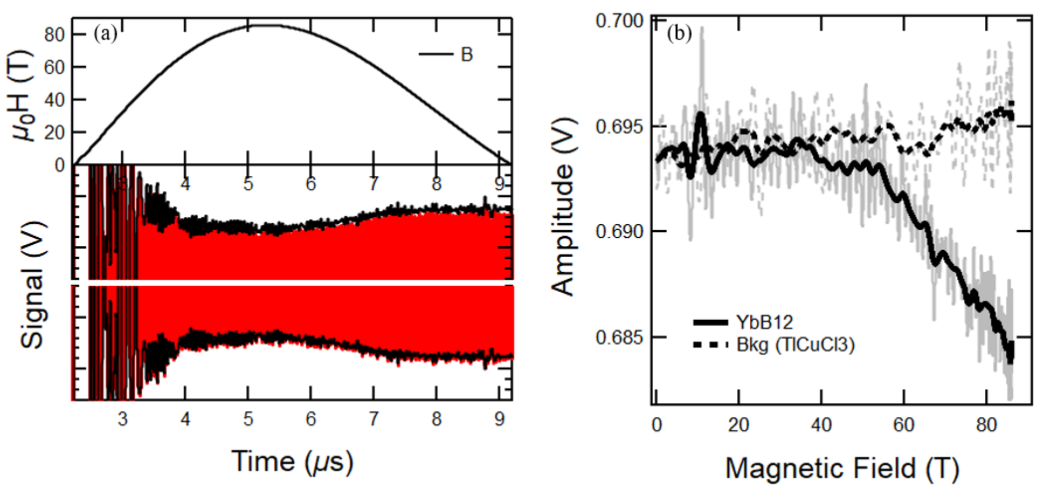

Figure 6.12: Magnetoresistance measured up to 80 T; (a) time dependence of the RF signal and magnetic field, (b) field dependence of amplitude signal by lock-in process from (a).

By using I-type coil, the magnetoresistance are measured up to 80 T, as shown in figure 6.12. The measurement are performed at 2 K. The time dependence of RF signal is shown as red curve in figure 6.12 (a). The amplitude of RF signals was obtained from lock-in technique. The field dependence of amplitude of RF signals are shown in 6.12 (b). The black solid curve are from the measurement of sample YbB_{12}. The black dash curves are from $TlCuCl_3$, that the magnetoresistance is not expected. A clear kink is observed around 50 T in the results of YbB_{12}.

Similar experiments are performed three times totally. The second and third experiment are performed up to 100 T and 120 T, respectively. In that case, the size of I-type coil is too large to insert into the cryostat compatible with single-coil for generating a magnetic field over 100 T. Therefore, II-type coil is employed in the second and third measurement.

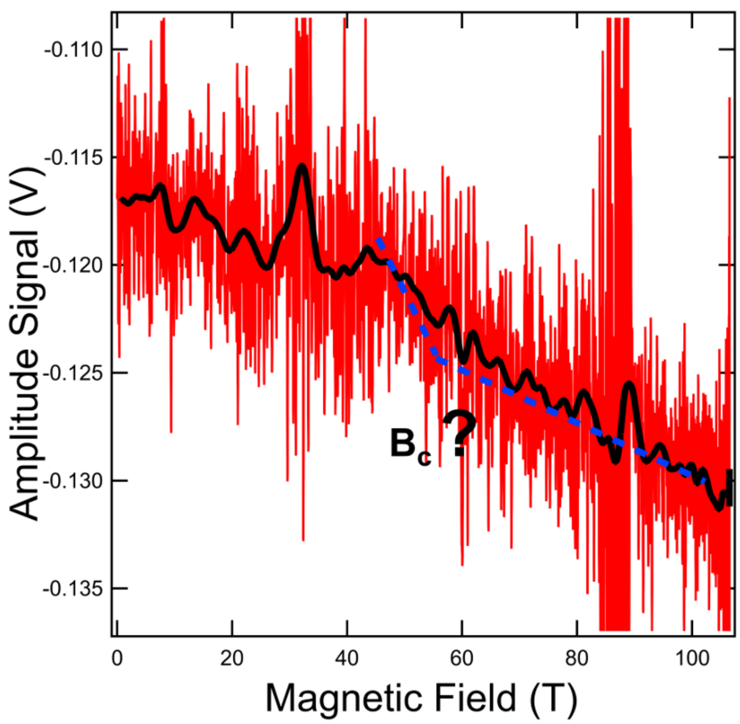

Figure 6.13: Field dependence of amplitude signal up to 100 T.

Figure 6.13 shows the measured results up to 102 T. The experiment are performed at 4.2 K. Because of the selected frequency is different with the first time, the amplitude signal show increasing with magnetic field. A similar kink is observed at around 50 T, which is consistent with the measurement up to 80 T. Here, I don't discuss the results of first and second experiment because of the magnetic field is not enough to observe the two-steps phase transition, although the kinks observed around 50 T indicate that the first phase transition is measured.

By employing the II-type coil, the magnetoresistance was measured up to 122 T at 4.2 K. Figure 6.14 shows the time dependence of the radio frequency (RF) signal at 430 MHz. Because the single-turn coil technique is employed, the noise is very large for the process of field up-sweep, where the RF observation signals are completely covered. Therefore, we only analyse the data of field down-sweep. In this experiment, we used the powder sample to avoid the joule heat problem. The environment heat is expected to be rapidly transmitted to the samples, so there can be only a small difference between the data of up-sweep and down sweep. Focusing on the process of down-sweep, continuous upward slope is clear. The blue curve is the amplitude RF signal obtained by lock-in detection. Although the noise problem is still very serious, the two kinks marked by arrows are clearly observed.

Figure 6.15 shows the magnetic field dependence of amplitude signals. Only amplitude signals of down-sweep field are shown here. The amplitude signal significantly decreased continuously below 40 T. The amplitude signal exhibits a hill-like shape from 20 T to 40 T, which is consistent with the previous report by F. Iga et al., shown as red open circles. Around 40 T to 100 T, the amplitude signal shows a plateau. It is also similar with F. Iga et al.'s data which exhibited a 40 T-70 T plateau. The amplitude signal decreased again at 100 T. We note that the decline has been very slight.

Since the resistance measurement results by F. Iga et al. [70] were surprisingly consistent with our results, we use the conductivity scaling of F. Iga et al. (left axis) here. The magnetoresistance decreased by about 0.05 (Ω cm) at B_{c2}. The absolute resistivity value is about 0.01 (Ω cm). Based on the theoretical study by T. Ohashi et. al [37], there are two-step phase transition from Kondo insulator to the paramagnetic metal, which is a KIS-KMS-NMS transition introduced in Sec. 2.3. The previous Terashima's magnetization measurements have proved that there is a phase transition at 100 T, which is consistent with our magnetoresistance measurement. Although the absolute resistivity is still higher than the high temperature resistivity of YbB_{12}, which is about 10^{-4} (Ω cm), the change of resistivity at this phase transition is confirmed by this measurement. It indicate that YbB_{12} has translated into a paramagnetic metal state, if there are no further phase transition in higher magnetic field (>120 T).

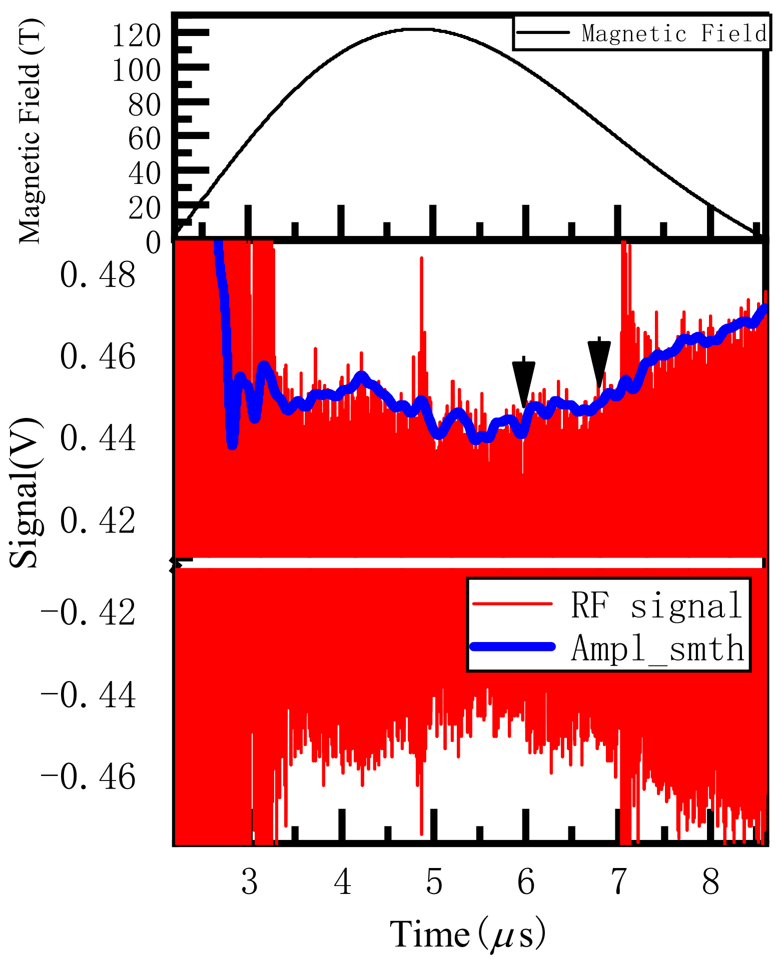

Figure 6.14: The time dependence of the RF signal

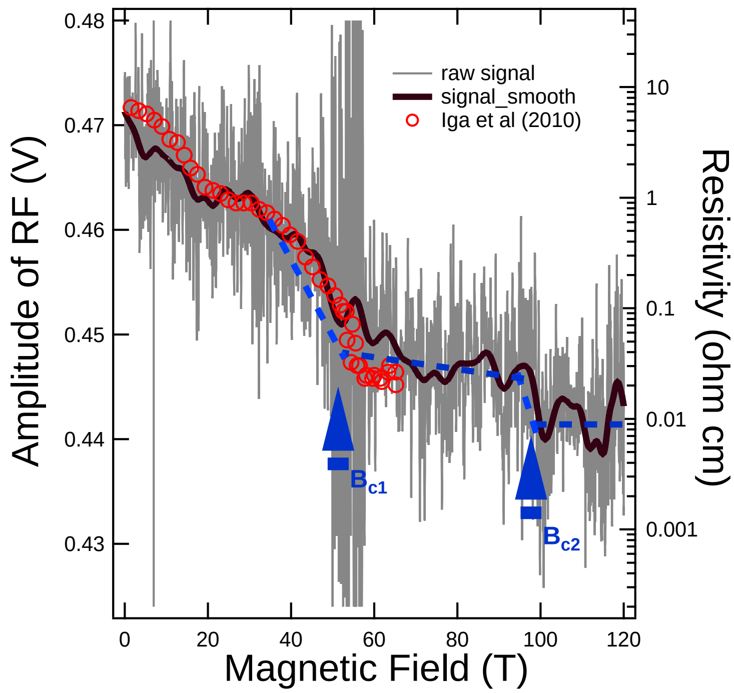

Figure 6.15: The field dependence of amplitude signal. Red open circle is from Ref. [70]

6.3 summary

In summary, I have measured the electric resistance of powdered YbB_{12} up to 120 T for the first time. The results show that the resistivity at 120 T is still on the order of 10^{-2} (Ω cm), which is higher than the resistivity of 10^{-4} (Ω cm) in the normal paramagnetic metal phase at high temperatures. This experimental finding suggests that the c-f hybridization is still dominant and the Kondo effect is significant at the second critical field around 100 T, even though a gradual breaking of the Kondo coupling begins. A stronger magnetic field can diminish the Kondo coupling completely and the corresponding magnetization as large as 4 μ_B will be induced. Our observations provide a reference for explaining the mechanism of formation of the Kondo insulator. Although the formation of the energy gap is a result of the strong electron correlation, the magnetic-field-induced closing of the energy gap little affect the Kondo coupling. Further study with multi-megagauss fields would reveal the entire process of the Kondo break down in YbB_{12}. From the technical point of view, our method of measuring electric resistance of a powder sample can also be extended to other various intriguing metal-insulator phase transition candidates.

Chapter 7

Conclusion

In this study, I have studied three correlated spin systems (CSSs), namely $TlCuCl_3$, α-$RuCl_3$ and YbB_{12} that exhibit significant quantum phenomena. Each of them has a strong correlation between spins and thus a strong magnetic field is necessary for unveiling the nature of its magnetic properties. In the present study, I have used an ultrahigh magnetic field exceeding 100 T (a megagauss magnetic field) that is produced by a destructive means, the vertical-type single-turn coil in the Institute for Solid State Physics, the University of Tokyo.

The magnetization process (M-H curve) of $TlCuCl_3$ was measured and the Bose-Einstein condensation (BEC) of magnons has been observed as the continuous-increase region between the gapped zero magnetization and the saturated magnetization phases. The second critical magnetic field (H_{c2}) has been firstly determined to be 86.1 T. A strong contrast of the lower $H_{c1} = 6$ T and the higher $H_{c2} = 86.1$ T critical fields indicates the strong inter-dimer interaction. A striking feature found in the M-H curve is an asymmetry with respect to the middle point of the critical fields, $(H_{c1} + H_{c2})/2$. At the beginning of the BEC, the particle density increases rather slowly with increasing magnetic field from H_{c1}, while at near the saturation, the hole density increases more rapidly with decreasing field from H_{c2}. Detailed analysis with Monte-Carlo calculations leads me to conclude that the asymmetric M-H curve is due to a particle-hole symmetry breaking in the magnon condensation. The hybirdization between the singlet and triplet states of a dimer in a magnetic field prevent the hard-core boson model being applicable, which results in breaking of the particle-hole symmetry.

In α-$RuCl_3$, the Kitaev spin liquid state is expected to appear when the non-Kitaev type antiferromagnetic interaction is suppressed. Applying magnetic fields is one of the most intriguing experiments and many of studies on properties in magnetic fields have been extensively conducted. Interestingly, the magnetization process has strong anisotropy and the characteristic magnetic-field-angle dependence of phase boundaries between different phases potentially including the spin-liquid phase has been theoretically proposed. In this study, the field-angle (θ) dependence of the magnetization process has been measured in high magnetic fields at 4.2 K. In addition to an observation of the significant field angle dependence of the magnetization, the saturation of magnetization for α-$RuCl_3$ is first observed for field perpendicular to the ab-plane ($\theta = 90°$). Also, I found three critical magnetic fields corresponding to the phase boundaries of the intermediate phases. The $\theta-$field (H) phase diagram is constructed based on the θ dependence of the critical magnetic fields. The field-induced intermediate phases probably be related to the spin liquid state. The obtained $\theta - H$ phase diagram can help to determine the full-spin Hamiltonian of α-$RuCl_3$.

I have studied the Kondo insulator YbB_{12} with the motivation that it is important to uncover the electronic state in a strong magnetic fields where the Kondo effect is suppressed. Although the successive two magnetic field-induced phase transitions in YbB_{12} were reported at 50 and 100 T with the magnetization process, the nature of the higher field phase has been unknown. Considering that the first 50 T-transition is due to the change from the Kondo insulator to the Kondo metal, the higher transition is potentially the transition from the Kondo metal to the normal metal with break down of the Kondo effect. The magnetoresistance measurement has been conduced using a developed contactless- high-frequency-modulation resistivity-measurement technique in a high magnetic field of up to 120 T. A small decrease of the electric resistivity has been observed at 100 T where the second transition takes place. The small change indicates the beginning of break down of the Kondo effect. The considerable weight of the density of the states (DOS), however, can be still away from the Fermi level, i.e., a higher magnetic field is required to completely suppress the Kondo effect and full DOS of the conduction electrons restore at the Fermi level. The detailed magnetic field dependence of the resistivity is expected to unveil the way of the Kondo breakdown and will be studied in near future with ultrahigh fields exceeding 300 T by the electromagnetic flux compression field generator.

The significant magnetic-field-induced phenomena in the three different CSSs have been investigated and it has been proved that a very strong magnetic field of 100 T class is essentially important to observe the phenomena because the magnetic field needs to compete the strong correlation. Since the various kinds of quantum phenomena are expected to be observed in the strong fields at a low temperature where the entropy is negligibly small, it is believed that the ultrahigh magnetic field study of the condensed matter physics will be further developed.

Bibliography

[1] W. Ketterle, D. Durfee, and D. Stamper-Kurn, *Proceedings of the International School of Physics Enrico Fermi, Course* **140**, 67 (1999).

[2] T. Matsubara and H. Matsuda, Progress of Theoretical Physics **16**, 569 (1956).

[3] T. Nikuni, M. Oshikawa, A. Oosawa, and H. Tanaka, Phys. Rev. Lett. **84**, 5868 (2000).

[4] G. Misguich and M. Oshikawa, Journal of the Physical Society of Japan **73**, 3429 (2004).

[5] F. Yamada, T. Ono, H. Tanaka, G. Misguich, M. Oshikawa, and T. Sakakibara, Journal of the Physical Society of Japan **77**, 013701 (2008).

[6] A. Rakhimov, E. Y. Sherman, and C. K. Kim, Phys. Rev. B **81**, 020407 (2010).

[7] E. Y. Sherman, P. Lemmens, B. Busse, A. Oosawa, and H. Tanaka, Phys. Rev. Lett. **91**, 057201 (2003).

[8] T. Giamarchi, C. Ruegg, and O. Tchernyshyov, NAT. Phys. **4**, 198 (2008).

[9] N. Johannsen, A. Vasiliev, A. Oosawa, H. Tanaka, and T. Lorenz, Phys. Rev. Lett. **95**, 017205 (2005).

[10] H. Tanaka, A. Oosawa, T. Kato, H. Uekusa, Y. Ohashi, K. Kakurai, and A. Hoser, Journal of the Physical Society of Japan **70**, 939 (2001).

[11] O. Nohadani, S. Wessel, B. Normand, and S. Haas, Phys. Rev. B **69**, 220402 (2004).

[12] N. Kawashima, Journal of the Physical Society of Japan **74**, 145 (2005).

[13] A. A. Aczel, Y. Kohama, M. Jaime, K. Ninios, H. B. Chan, L. Balicas, H. A. Dabkowska, and G. M. Luke, Phys. Rev. B **79**, 100409 (2009).

[14] A. A. Aczel, Y. Kohama, C. Marcenat, F. Weickert, M. Jaime, O. E. Ayala-Valenzuela, R. D. McDonald, S. D. Selesnic, H. A. Dabkowska, and G. M. Luke, Phys. Rev. Lett. **103**, 207203 (2009).

[15] M. Matsumoto, B. Normand, T. M. Rice, and M. Sigrist, Phys. Rev. Lett. **89**, 077203 (2002).

[16] B. Leon, Nature **464**, 199 (2010).

[17] S. Lucile and B. Leon, Reports on Progress in Physics **80**, 016502 (2017), arXiv:1601.03742 [cond-mat.str-el] .

[18] P. Anderson, Materials Research Bulletin **8**, 153 (1973).

[19] D. A. Huse and V. Elser, Physical Review Letters **60**, 2531 (1988).

[20] L. B. Ioffe and A. I. Larkin, Physical Review B **39**, 8988 (1989).

[21] N. Nagaosa and P. A. Lee, Physical Review Letters **64**, 2450 (1990).

[22] A. Olariu, P. Mendels, F. Bert, F. Duc, J. C. Trombe, M. A. de Vries, and A. Harrison, Physical Review Letters .

[23] A. Kitaev, Annals of Physics **321**, 2 (2006), arXiv:cond-mat/0506438 [cond-mat.mes-hall] .

[24] H. Takagi, T. Takayama, G. Jackeli, G. Khaliullin, and S. E. Nagler, Nature Reviews Physics **1**, 264 (2019).

[25] Y. Motome and J. Nasu, Journal of the Physical Society of Japan **89**, 012002 (2020), https://doi.org/10.7566/JPSJ.89.012002 .

[26] J. c. v. Chaloupka, G. Jackeli, and G. Khaliullin, Phys. Rev. Lett. **110**, 097204 (2013).

[27] R. D. Johnson, S. C. Williams, A. A. Haghighirad, J. Singleton, V. Zapf, P. Manuel, I. I. Mazin, Y. Li, H. O. Jeschke, R. Valentí, and R. Coldea, Phys. Rev. B **92**, 235119 (2015).

[28] Y. Kubota, H. Tanaka, T. Ono, Y. Narumi, and K. Kindo, Phys. Rev. B **91**, 094422 (2015).

[29] J. Kondo, Progress of Theoretical Physics **32**, 37 (1964), https://academic.oup.com/ptp/article-pdf/32/1/37/5193092/32-1-37.pdf .

[30] P. W. Anderson, Phys. Rev. **124**, 41 (1961).

[31] K. Miyake, T. Matsuura, and C. Varma, Solid state communications **71**, 1149 (1989).

[32] A. Jacko, J. Fjærestad, and B. Powell, Nature Physics **5**, 422 (2009).

[33] A. Menth, E. Buehler, and T. Geballe, Physical Review Letters **22**, 295 (1969).

[34] M. Hundley, P. Canfield, J. Thompson, Z. Fisk, and J. Lawrence, Physical Review B **42**, 6842 (1990).

[35] T. Takabatake, F. Teshima, H. Fujii, S. Nishigori, T. Suzuki, T. Fujita, Y. Yamaguchi, J. Sakurai, and D. Jaccard, Physical Review B **41**, 9607 (1990).

[36] M. Kasaya, F. Iga, K. Negishi, S. Nakai, and T. Kasuya, Journal of Magnetism and Magnetic Materials **31**, 437 (1983).

[37] T. Ohashi, A. Koga, S.-i. Suga, and N. Kawakami, Physical Review B **70**, 245104 (2004).

[38] T. T. Terashima, A. Ikeda, Y. H. Matsuda, A. Kondo, K. Kindo, and F. Iga, Journal of the Physical Society of Japan **86**, 054710 (2017).

[39] N. Miura, Physica B: Condensed Matter **201**, 40 (1994).

[40] S. Takeyama, R. Sakakura, Y. H. Matsuda, A. Miyata, and M. Tokunaga, Journal of the Physical Society of Japan **81**, 014702 (2011).

[41] T. Sekitani, Y. Matsuda, S. Ikeda, K. Uchida, F. Herlach, N. Miura, K. Nakao, T. Izumi, S. Tajima, M. Murakami, et al., Physica C: Superconductivity **392**, 116 (2003).

[42] M. Jaime, V. F. Correa, N. Harrison, C. D. Batista, N. Kawashima, Y. Kazuma, G. A. Jorge, R. Stern, I. Heinmaa, S. A. Zvyagin, Y. Sasago, and K. Uchinokura, Phys. Rev. Lett. **93**, 087203 (2004).

[43] F. Mila, Eur. Phys. J. B **6**, 201 (1998).

[44] H.-T. Wang, B. Xu, and Y. Wang, Journal of Physics: Condensed Matter **18**, 4719 (2006).

[45] M. Matsumoto, B. Normand, T. M. Rice, and M. Sigrist, Phys. Rev. B **69**, 054423 (2004).

[46] A. Oosawa, M. Ishii, and H. Tanaka, Journal of Physics: Condensed Matter **11**, 265 (1999).

[47] V. Zapf, M. Jaime, and C. Batista, Reviews of Modern Physics **86**, 563 (2014).

[48] Y. H. Matsuda, N. Abe, S. Takeyama, H. Kageyama, P. Corboz, A. Honecker, S. R. Manmana, G. R. Foltin, K. P. Schmidt, and F. Mila, Phys. Rev. Lett. **111**, 137204 (2013).

[49] S. Takeyama, R. Sakakura, Y. H. Matsuda, A. Miyata, and M. Tokunaga, J. Phys. Soc. Jap. **81**, 014702 (2012).

[50] X.-G. Zhou, Y. Yao, Y. Matsuda, A. Ikeda, A. Matsuo, K. Kindo, and H. Tanaka, Physical Review Letters **125**, 267207 (2020).

[51] A. Oosawa, H. A. Katori, and H. Tanaka, Phys. Rev. B **63**, 134416 (2001).

[52] F. Alet, S. Wessel, and M. Troyer, Phys. Rev. E **71**, 036706 (2005).

[53] A. Albuquerque, F. Alet, P. Corboz, P. Dayal, A. Feiguin, S. Fuchs, L. Gamper, E. Gull, S. Gürtler, A. Honecker, R. Igarashi, M. Körner, A. Kozhevnikov, A. Läuchli, S. Manmana, M. Matsumoto, I. McCulloch, F. Michel, R. Noack, G. Pawłowski, L. Pollet, T. Pruschke,

U. Schollwöck, S. Todo, S. Trebst, M. Troyer, P. Werner, and S. Wessel, Journal of Magnetism and Magnetic Materials **310**, 1187 (2007), proceedings of the 17th International Conference on Magnetism.

[54] S. Hayashida, D. Blosser, K. Y. Povarov, Z. Yan, S. Gvasaliya, A. N. Ponomaryov, S. A. Zvyagin, and A. Zheludev, Phys. Rev. B **100**, 134427 (2019).

[55] J. Brambleby, P. A. Goddard, J. Singleton, M. Jaime, T. Lancaster, L. Huang, J. Wosnitza, C. V. Topping, K. E. Carreiro, H. E. Tran, Z. E. Manson, and J. L. Manson, Phys. Rev. B **95**, 024404 (2017).

[56] Y. Kohama, A. V. Sologubenko, N. R. Dilley, V. S. Zapf, M. Jaime, J. A. Mydosh, A. Paduan-Filho, K. A. Al-Hassanieh, P. Sengupta, S. Gangadharaiah, A. L. Chernyshev, and C. D. Batista, Phys. Rev. Lett. **106**, 037203 (2011).

[57] A. Banerjee, C. A. Bridges, J.-Q. Yan, A. A. Aczel, L. Li, M. B. Stone, G. E. Granroth, M. D. Lumsden, Y. Yiu, J. Knolle, S. Bhattacharjee, D. L. Kovrizhin, R. Moessner, D. A. Tennant, D. G. Mandrus, and S. E. Nagler, Nature Materials **15**, 733 (2016).

[58] S.-H. Do, S.-Y. Park, J. Yoshitake, J. Nasu, Y. Motome, Y. S. Kwon, D. T. Adroja, D. J. Voneshen, K. Kim, T.-H. Jang, J.-H. Park, K.-Y. Choi, and S. Ji, Nature Physics **13**, 1079 (2017).

[59] A. Banerjee, P. Lampen-Kelley, J. Knolle, C. Balz, A. A. Aczel, B. Winn, Y. Liu, D. Pajerowski, J. Yan, C. A. Bridges, A. T. Savici, B. C. Chakoumakos, M. D. Lumsden, D. A. Tennant, R. Moessner, D. G. Mandrus, and S. E. Nagler, npj Quantum Materials **3**, 8 (2018).

[60] C. Wellm, J. Zeisner, A. Alfonsov, A. U. B. Wolter, M. Roslova, A. Isaeva, T. Doert, M. Vojta, B. Büchner, and V. Kataev, Phys. Rev. B **98**, 184408 (2018).

[61] Y. Kasahara, T. Ohnishi, Y. Mizukami, O. Tanaka, S. Ma, K. Sugii, N. Kurita, H. Tanaka, J. Nasu, Y. Motome, T. Shibauchi, and Y. Matsuda, Nature **559**, 227 (2018).

[62] K. A. Modic, R. D. McDonald, J. P. C. Ruff, M. D. Bachmann, Y. Lai, J. C. Palmstrom, D. Graf, M. K. Chan, F. F. Balakirev, J. B. Betts,

G. S. Boebinger, M. Schmidt, M. J. Lawler, D. A. Sokolov, P. J. W. Moll, B. J. Ramshaw, and A. Shekhter, Nature Physics 10.1038/s41567-020-1028-0 (2020).

[63] K. Riedl, Y. Li, S. M. Winter, and R. Valentí, Phys. Rev. Lett. **122**, 197202 (2019).

[64] Y.-F. Jiang, T. P. Devereaux, and H.-C. Jiang, Phys. Rev. B **100**, 165123 (2019).

[65] K. Sugiyama, F. Iga, M. Kasaya, T. Kasuya, and M. Date, Journal of the Physical Society of Japan **57**, 3946 (1988), https://doi.org/10.1143/JPSJ.57.3946 .

[66] F. Iga, N. Shimizu, and T. Takabatake, Journal of Magnetism and Magnetic Materials **177-181**, 337 (1998), international Conference on Magnetism.

[67] J. Yamaguchi, A. Sekiyama, S. Imada, H. Fujiwara, M. Yano, T. Miyamachi, G. Funabashi, M. Obara, A. Higashiya, K. Tamasaku, M. Yabashi, T. Ishikawa, F. Iga, T. Takabatake, and S. Suga, Phys. Rev. B **79**, 125121 (2009).

[68] Y. H. Matsuda, Y. Murata, T. Inami, K. Ohwada, H. Nojiri, K. Ohoyama, N. Katoh, Y. Murakami, F. Iga, T. Takabatake, A. Mitsuda, and H. Wada, Journal of Physics: Conference Series **51**, 490 (2006).

[69] M. Okawa, Y. Ishida, M. Takahashi, T. Shimada, F. Iga, T. Takabatake, T. Saitoh, and S. Shin, Phys. Rev. B **92**, 161108 (2015).

[70] F. Iga, K. Suga, K. Takeda, S. Michimura, K. Murakami, T. Takabatake, and K. Kindo, Journal of Physics: Conference Series **200**, 012064 (2010).

[71] T. T. Terashima, A. Ikeda, Y. H. Matsuda, A. Kondo, K. Kindo, and F. Iga, Journal of the Physical Society of Japan **86**, 054710 (2017), https://doi.org/10.7566/JPSJ.86.054710 .